The Cryosphere Discuss., 7, 4321–4377, 2013
www.the-cryosphere-discuss.net/7/4321/2013/
doi:10.5194/tcd-7-4321-2013

The Cryosphere
Discussions
Open Access

Sea ice and the ocean mixed layer over the Antarctic shelf seas

A. A. Petty[1], P. R. Holland[2], and D. L. Feltham[3]

[1]Centre for Polar Observation and Modelling, Department of Earth Sciences, University College London, London, WC1E 6BT, UK
[2]British Antarctic Survey, High Cross, Madingley Road, Cambridge CB3 0ET, UK
[3]Centre for Polar Observation and Modelling, Department of Meteorology, University of Reading, Reading, RG6 6BB, UK

Received: 15 August 2013 – Accepted: 21 August 2013 – Published: 30 August 2013

Correspondence to: A. A. Petty (alek.petty.10@ucl.ac.uk)

Published by Copernicus Publications on behalf of the European Geosciences Union.

Abstract

An ocean mixed layer model has been incorporated into the Los Alamos sea ice model CICE to investigate regional variations in the surface-driven formation of Antarctic shelf waters. This model captures well the expected sea ice thickness distribution, and produces deep (> 500 m) mixed layers in the Weddell and Ross shelf seas each winter. This results in the complete destratification of the water column in deep southern coastal regions (leading to HSSW formation) and also in some shallower regions (no HSSW formation) of these seas. Shallower mixed layers are produced in the Amundsen and Bellingshausen seas. By deconstructing the surface power input to the mixed layer, we show that the freshwater flux from sea ice growth/melt dominates the evolution of the mixed layer in all seas, with a smaller contribution from the surface heat flux. The Weddell and Ross shelf seas receive an annual surplus of energy at the surface, the Amundsen shelf sea energy input in autumn/winter is balanced by energy extraction in spring/summer, and the Bellingshausen shelf sea experiences an annual surface energy deficit, through both a low energy input in autumn/winter and the highest energy loss in spring/summer. An analysis of the sea ice mass balance demonstrates the contrasting mean ice growth, melt and export in each region. The Weddell and Ross shelf seas have the highest annual ice growth, with a large fraction exported northwards each year, whereas the Bellingshausen shelf sea experiences the highest annual ice melt, driven by the advection of ice from the northeast. A linear regression analysis is performed to determine the temporal and spatial correlations between the autumn/winter mixed layer power input and several atmospheric variables. The temporal mean Weddell and Ross autumn/winter power input shows stronger spatial correlation to several atmospheric variables compared to the Amundsen and Bellingshausen. In contrast the spatial mean autumn/winter power input shows stronger temporal correlation to several atmospheric variables, in the Amundsen and Bellingshausen. All regions show strong temporal correlation between the autumn/winter surface power input and the meridional wind speed except the Ross, which instead shows moderate

TCD
7, 4321–4377, 2013

correlation to the zonal wind speed. Further regressions demonstrate that this is probably due to the Ross shelf-sea geometry and impact of the ocean turning angle on ice motion, with a more zonal (eastward) wind preventing ice build up along the Cape Adare coast in the eastern Ross shelf sea, increasing ice export.

1 Introduction

The continental shelf seas surrounding West Antarctica are a crucial component of the Earth's climate system, with the Weddell and Ross (WR) shelf seas cooling and ventilating the deep ocean (Orsi et al., 2001) and feeding the global thermohaline circulation (Orsi et al., 1999; Jacobs, 2004), whereas the Amundsen and Bellingshausen (AB) shelf seas are implicit in the recent ocean-driven melting of the Antarctic Ice Sheet (Shepherd et al., 2004; Holland et al., 2010; Jacobs et al., 2011; Fricker and Padman, 2012; Pritchard et al., 2012; Rignot et al., 2013). This contrast in the behaviour of the shelf seas is most apparent in the clear bimodal distribution of the ocean temperature at the shelf seabed (Fig. 1), which is a result of cold, saline, oxygen-rich shelf waters (at around the surface freezing temperature of $\sim -1.9\,^{\circ}$C) filling the WR shelf seas (Jacobs et al., 1970; Gill, 1973; Nicholls et al., 2009; Orsi and Wiederwohl, 2009), and Circumpolar Deep Water (CDW), which is warm ($+1\,^{\circ}$C), slightly less saline, and deoxygenated, flooding onto the AB shelf seas (Talbot, 1988; Jacobs et al., 1996, 2011; Jenkins and Jacobs, 2008; Martinson et al., 2008).

The brine rejection from sea ice growth in the WR shelf seas causes a salinification and deepening of the surface mixed layer, resulting in the formation of High Salinity Shelf Water (HSSW) through the complete destratification of the water column (where the surface mixed layer extends to the seabed), with the HSSW residing on the shelf for several years (Gill, 1973). In the Weddell Sea, HSSW is either advected northwards, crossing the shelf break (Gill, 1973; Foster and Carmack, 1976; Gordon et al., 1993), or it enters the Filchner–Ronne Ice Shelf cavity to the south, producing Ice Shelf Water (ISW) as the HSSW melts the base of the ice shelf. The ISW is eventually transported north of the shelf through the Filchner depression (Foldvik et al., 2004; Wilchinsky and Feltham, 2009). A similar process takes place in the Ross Sea, where HSSW is either transported northwards past the Ross continental shelf break (Jacobs et al., 1970; Orsi et al., 1999) or is transported southwards into the Ross Ice Shelf cavity, with the resulting ISW flowing northwards through the eastern shelf sea (Jacobs et al., 1970, 1985). The eventual transport of the HSSW off the shelf results in the formation of Weddell Sea Bottom Water (WSBW) and Ross Sea Bottom Water (RSBW) (Orsi et al., 1999; Jacobs, 2004) which, together with Adélie Land Bottom Water (ALBW) (Williams et al., 2010) and the more recently discovered Cape Darnley Bottom Water (CDBW) (Ohshima et al., 2013), form Antarctic Bottom Water (AABW), which drives the bottom cell of the global thermohaline circulation, that accounts for around a third of the total ocean volume (Johnson, 2008).

While ALBW and CDBW are fed by HSSW formed as a result of rapid brine release from small coastal polynyas over a narrow continental shelf region, the HSSW source of WSBW and RSBW is formed through a combination of rapid sea ice growth in coastal polynyas and a more gradual sea ice growth over a broader continental shelf. In the Weddell Sea, the gradual brine release over the shelf is thought to be the dominant mechanism of converting Modified Warm Deep Water (MWDW) entering the shelf to HSSW (Renfrew et al., 2002; Nicholls et al., 2009). In the Ross Sea, the coastal polynyas produce significantly more sea ice (both in volume and as a fraction of the ice exported out of the shelf, Drucker et al., 2011), although it is expected the remaining sea ice growth plays a similar role to that in the Weddell Sea. The relative size and impact of the coastal polynyas in the two regions is thought to be driven by the difference in the near-surface winds, with low pressure systems leading to strong southerly winds in the Ross Sea, and weaker southeasterly winds in the Weddell Sea (see Fig. 2). As well as these low pressure systems, the WR seas also experience the coldest ($\sim -25\,^{\circ}$C) near-surface air temperatures over the Antarctic continental shelf in winter, due to strong katabatic winds carrying cold air to the WR coastlines from the centre of Antarctica (van Lipzig et al., 2004), which is also thought to play a key role in sea ice production and the resultant shelf water formation. As a result of these dense shelf waters, the Filchner–Ronne Ice Shelf (FRIS) in the Weddell Sea and the Ross Ice Shelf (RIS) in the Ross Sea, are relatively well protected from the warm waters residing offshore in the Antarctic Circumpolar Current (ACC).

In contrast the AB shelf seas experience warmer ($\sim -15\,^{\circ}$C) surface air temperatures in winter, which, along with several other atmospheric differences, was demonstrated by Petty et al. (2012) to be sufficient to explain the lack of shelf water formation in these two regions. The difference in shelf-water properties may also be explained by the proximity of warm CDW from the southern boundary of the ACC, which is situated just offshore of the shelf break in these regions. In the AB shelf seas, CDW is overlain by Winter Water (WW) formed from the remnants of winter mixed layers, which do not extend to the seabed here. The Bellingshausen Sea is thought to be flooded by CDW as eddies from the ACC are shed onto the shelf (Martinson and McKee, 2012), although other mechanisms have been presented, e.g. Klinck et al. (2004). In the Amundsen Sea, seasonal wind pulses drive transport of CDW into glacially-carved troughs in the continental shelf (Walker et al., 2007; Thoma et al., 2008; Wåhlin et al., 2010; Arneborg et al., 2012). The variability of this warm CDW layer has been implicated in the recent rapid thinning of the ice shelves in the Amundsen and Bellingshausen seas (Shepherd et al., 2004; Holland et al., 2010; Jacobs et al., 2011; Fricker and Padman, 2012; Pritchard et al., 2012; Rignot et al., 2013). Variability in the thickness of the CDW layer can either be driven by variable upwelling at the shelf break (Thoma et al., 2008) or by variable mixing of cold waters from above (Holland et al., 2010). An understanding of the formation of waters overlying the CDW is therefore important in understanding future ice loss from the Antarctic Ice Sheet.

Modelling studies have demonstrated the crucial role of sea ice in controlling the upper ocean characteristics of the Bellingshausen (Meredith et al., 2004; Holland et al., 2010) and Amundsen (Assmann et al., 2005) seas, and in the formation of shelf waters in the Weddell (Timmermann et al., 2002) and Ross (Assmann and Timmermann, 2005) seas. Despite these regional modelling studies, to our knowledge a consistent

TCD
7, 4321–4377, 2013

modelling approach to all four shelf sea regimes has yet to be undertaken. This study seeks to build on these earlier approaches by using a sophisticated sea ice model to study how regional differences in the atmosphere and sea ice might control the mixed layer evolution in these four important climatic regions.

The paper is structured as follows: Sect. 2 presents the model formulation; Sect. 3 discusses the model results; and concluding remarks are given in Sect. 4.

2 Model Formulation

In this study a variable mixed-layer ocean model is incorporated into the Los Alamos sea ice model CICE (version 4.1). The standard CICE configuration includes five ice thickness categories, one snow thickness category and open water. The sea ice thermodynamics are based on Bitz and Lipscomb (1999) which takes into account internal brine pockets within the sea ice and is an energy-conserving update to the Maykut and Untersteiner (1971) sea ice surface energy balance. The ice dynamics are based on the viscous-plastic (VP) rheology of Hibler (1979), updated to the more numerically efficient elastic-viscous-plastic (EVP) rheology of Hunke and Dukowicz (1997). A full description of the Los Alamos CICE sea ice model can be found in its user manual (Hunke and Lipscomb, 2008).

In the standard CICE configuration, the mixed-layer depth is set to a constant value (default of 30 m), the mixed-layer salinity is prescribed, and the mixed-layer temperature is prognostic, with the option of restoring this temperature towards data. A deep ocean-mixed layer heat flux is prescribed from data. By adapting CICE to include a variable mixed layer, we allow the mixed layer depth, temperature and salinity to evolve, based on the calculated surface and deep-ocean fluxes as described below.

We use a bulk mixed layer model based on Kraus and Turner (1967) and Niiler and Kraus (1977), similar to that described in Petty et al. (2012). The use of a simple bulk mixed layer reduces the computational cost of studying the formation of shelf waters, and enables us to have a complete understanding of all aspects of the model results. The ocean below the mixed layer is relaxed towards observations, rather than modelled, which allows us to remove the impact of variable ocean dynamics and thus isolate the effect of surface forcings.

The sea ice has been adapted substantially from that of Petty et al. (2012), so the following section discusses the CICE-mixed layer model that has been developed. The mixed-layer model has no horizontal interaction, so the description below applies to each grid cell within CICE. Constants and fixed parameters referred to in this section are listed in Table 1.

2.1 Model Description

2.1.1 Heat and Salt Fluxes

While CICE treats the mixed layer and surface layer as analogous, we use a simple 2-layer ocean for our temperature calculations, consisting of a fixed depth ocean surface layer $h_S = 10\,\mathrm{m}$ and a variable mixed layer h_{mix} below, as shown in Fig. 3. The surface temperature layer exchanges heat with the variable-depth mixed layer below and with the sea ice and atmosphere above, as described later in this section. Adding this surface temperature layer allows to model the expected rapid change in temperature of the ocean surface, improving the fit of modelled ice concentration to observations, while still providing us with a simple and computationally efficient sea ice-mixed layer model to use for this study. Without this surface layer, the mixed layer and thus surface temperature often remained slightly above freezing when the mixed layer was deep (order of several hundred meters), hindering the formation of sea ice in winter. Note that for simplicity the salinity calculations ignore this surface layer and treat the mixed layer salinity and surface salinity as the same, as small changes in the surface salinity will not have the same impact on the sea ice growth and melt compared to surface temperature.

The heat flux into the ocean surface layer from the ice and open-ocean fractions (all fluxes are positive downwards) is calculated as

$$F_{\text{surface}} = (1 - A)\left(F^{\text{o}}_{\text{sens}} + F^{\text{o}}_{\text{lat}} + F^{\text{o}}_{\text{lwout}} + F^{\text{o}}_{\text{lw}} + F^{\text{o}}_{\text{swabs}}\right) + A(F_{\text{ice}} + F_{\text{swthru}}), \quad (1)$$

where $F^{\text{o}}_{\text{sens}}$ is the sensible heat flux between the atmosphere to the open-ocean surface, $F^{\text{o}}_{\text{lat}}$ is the latent heat flux between the atmosphere and the open-ocean surface, $F^{\text{o}}_{\text{lwout}}$ is the black-body heat flux from the open-ocean surface to the atmosphere, F^{o}_{lw} is the downward longwave radiative heat flux, $F^{\text{o}}_{\text{swabs}}$ is the downward shortwave radiative heat flux calculated as a sum over four radiative categories (direct and diffuse, visible and near-infrared) with varying albedo parameterisations, F_{ice} is the heat flux from the ocean surface to the base of the ice (aggregated over all ice categories/thicknesses), and F_{swthru} is the shortwave radiative heat flux that passes through the ice and is absorbed by the ocean. These are all shown schematically in Fig. 3 along with several other variables described below.

We calculate an ocean heat flux from the mixed layer to the surface layer as

$$F_{\text{ocean}} = c_p \rho_{\text{w}} u_\star (T_{\text{S}} - T_{\text{mix}}), \quad (2)$$

where T_{S} is the ocean surface temperature and T_{mix} is the mixed layer temperature. The surface layer is assumed to be in free-drift, meaning $u_\star$ is the ocean surface friction velocity, calculated through a combination of the ice-ocean wind stress τ_i and the open water wind stress τ_o as

$$u_\star = \sqrt{[A\tau_i + (1 - A)\tau_o]/\rho_{\text{w}}}. \quad (3)$$

We calculate the net salt flux (in m s^{-1}) into the mixed layer from the ice fraction as

$$F^{S}_{\text{ice}} = [(1000 - S_{\text{mix}})F_{\text{salt}} - S_{\text{mix}}F_{\text{fresh}}]A/\rho_{\text{w}}. \quad (4)$$

Discussion Paper | Discussion Paper | Discussion Paper | Discussion Paper |
TCD
7, 4321–4377, 2013
Antarctic sea ice and mixed layer
A. A. Petty et al.

where F_{salt} and F_{fresh} are the direct fluxes of salt and freshwater respectively (in kg $m^{-2}\,s^{-1}$), calculated by CICE as a combination of ice/snow growth/melt and snow lost to the mixed layer through pressure ridging.

The other source of freshwater that enters the mixed layer is from precipitation and evaporation. CICE reads in both rainfall and snowfall (changing rain to snow if $T_a \leq 0\,^{\circ}$C), giving a net freshwater flux of

$$F^S_{pe} = -\frac{S_{mix}}{\rho_w}[F_{rain} + (1-A)(F_{snow} + F^o_{lat}/L_v)], \tag{5}$$

where F_{rain} and F_{snow} are the prescribed rates of rainfall and snowfall. Note that rainfall on sea ice is assumed to percolate through the sea ice and enters the mixed layer.

2.1.2 Power Input

The rate of mechanical energy input to the mixed layer from surface buoyancy fluxes is given by a combination of the following: (i) salt/freshwater flux from sea ice growth/melt P_{salt}; (ii) salt/freshwater flux from precipitation and evaporation P_{pe}; (iii) the heat flux between the ocean surface layer and the mixed layer P_{heat}; and (iv) wind shearing from the ice and open water fractions P_{wind}. By splitting up the relative contributions to the surface power input we can analyse the impact of each term on the mixed layer evolution. The surface power inputs (per unit density, i.e. in$m^3\,s^{-3}$) are given respectively as

$$P_{salt} = c_B g \beta h_{mix} F^S_{ice}, \tag{6}$$

$$P_{pe} = c_B g \beta h_{mix} F^S_{pe}, \tag{7}$$

$$P_{heat} = -\frac{c_B g \alpha h_{mix}}{c_p \rho_w} F_{ocean}, \tag{8}$$

where h_{mix} is the mixed layer depth and

$$c_B = \exp(-h_{mix}/d_B) \tag{9}$$

is a variable parameter describing the fraction of energy that remains in the mixed layer after convective dissipative effects are taken into account. Note that to allow for the representation of deep (several hundred meters deep) mixed layers we choose $c_B \geq \exp(-h_B^{max}/d_B)$ following Lemke et al. (1990) where we have used a higher value of $h_B^{max} = 100$ m instead of the Lemke et al. (1990) value of 50 m, preventing a large Weddell polynya that forms every winter near the Greenwich Meridian. This is a region of observed low ice concentrations (Lindsay et al., 2004) which is due to a halo of warm waters encircling the Maud Rise at depths just below the mixed layer (de Steur et al., 2007); a process that is impossible to capture in our simple model.

The input of power from wind shearing is

$$P_{wind} = c_w u_\star^3, \tag{10}$$

where c_w is a depth-dependant dissipation coefficient for wind mixing, given by

$$c_w = \exp(-h_{mix}/d_w). \tag{11}$$

We also use the term P_{net}, which refers to the sum of the four surface power input terms described above.

2.1.3 Mixed Layer Entrainment

We use the bulk mixed layer energy balance formulation of Kraus and Turner (1967) and Niiler and Kraus (1977), which assumes that temperature and salinity are uniform throughout the mixed layer, and there is a full balance in the sources and sinks of turbulent kinetic energy (TKE) (See Petty et al. (2012) for further details about this model choice). While our precise definition of h_{mix} varies for salinity and temperature, we believe the error this introduces to the energy balance will have an insignificant impact on the results compared to the general assumptions made by the bulk mixed layer model. The mixed layer entrainment rate is calculated by balancing the energy needed to entrain water from below with the energy provided by the wind and the

TCD
7, 4321–4377, 2013

surface buoyancy fluxes which, when rearranged, gives the mixed layer entrainment rate as

$$\varpi = \frac{\mathrm{d}h_{\mathrm{mix}}}{\mathrm{d}t} = \frac{P_{\mathrm{net}}}{h_{\mathrm{mix}}\Delta b + c_m^2}, \tag{12}$$

where c_m is a bulk turbulent velocity scale representing the turbulent fluctuations of the mixed layer that will result in a frictional sink of TKE, and Δb is the difference in the buoyancy of the waters across the mixed layer base, given by

$$\Delta b = g\alpha(T_{\mathrm{mix}} - T_b) - g\beta(S_{\mathrm{mix}} - S_b), \tag{13}$$

where T_b and S_b are the deep ocean temperature and salinity respectively, which are both simple prognostic variables in this model (see Sect. 2.1.5).

This entrainment rate calculation is also used when $\varpi < 0$ to force the mixed layer to detrain back to a stable depth. We also use a minimum mixed layer depth such that $h_{\mathrm{mix}} \geq h_{\mathrm{min}}$. During detrainment the salinity and temperature is only updated through surface fluxes, leaving behind a layer of Winter Water. If the calculated mixed layer depth is greater than the seabed depth h_{bath} the entrainment rate is reduced such that the mixed layer depth equals the respective limit.

2.1.4 Temperature and Salinity Calculations

Through a combination of surface and entrainment heat/salt fluxes we calculate the changes in the mixed layer temperature and salinity as

$$\frac{\mathrm{d}T_{\mathrm{mix}}}{\mathrm{d}t} = \begin{cases} \frac{F_{\mathrm{ocean}}}{\rho_{\mathrm{w}} c_p h_{\mathrm{mix}}} + \frac{w}{h_{\mathrm{mix}}}(T_b - T_{\mathrm{mix}}) & w > 0 \\ \frac{F_{\mathrm{ocean}}}{\rho_{\mathrm{w}} c_p h_{\mathrm{mix}}} & w \leq 0, \end{cases} \tag{14}$$

$$\frac{\mathrm{d}S_{\mathrm{mix}}}{\mathrm{d}t} = \begin{cases} \frac{F^S_{\mathrm{ice}} + F^S_{\mathrm{pe}}}{h_{\mathrm{mix}}} + \frac{w}{h_{\mathrm{mix}}}(S_b - S_{\mathrm{mix}}) & \text{for } w > 0 \\ \frac{F^S_{\mathrm{ice}} + F^S_{\mathrm{pe}}}{h_{\mathrm{mix}}} & \text{for } w \leq 0, \end{cases} \tag{15}$$

and an ocean surface temperature change given by

$$\frac{\mathrm{d}T_{\mathrm{S}}}{\mathrm{d}t} = \frac{F_{\mathrm{surface}} - F_{\mathrm{ocean}}}{c_p \rho_{\mathrm{w}} h_{\mathrm{S}}}. \tag{16}$$

We compute the potential to freeze/melt ice in the surface layer as

$$H^S_{\mathrm{frzmlt}} = c_p \rho_{\mathrm{w}} h_{\mathrm{S}} (T_{\mathrm{f}} - T_{\mathrm{S}})/\mathrm{d}t, \tag{17}$$

after which we ensure $T_{\mathrm{S}} \geq T_{\mathrm{f}}$ such that any latent heat flux from ice formation is included in our heat flux calculations. In the case that $T_{\mathrm{mix}} < T_{\mathrm{f}}$ we compute the potential to form ice in the mixed layer (not melting as it is separated from the ice by the surface layer) as

$$H^{\mathrm{mix}}_{\mathrm{frzmlt}} = c_p \rho_{\mathrm{w}} h_{\mathrm{mix}} (T_{\mathrm{f}} - T_{\mathrm{mix}})/\mathrm{d}t \quad \text{for} \quad T_{\mathrm{mix}} < T_{\mathrm{f}} \tag{18}$$

in which case we set $T_{\mathrm{mix}} = T_{\mathrm{f}}$ to ensure $T_{\mathrm{mix}} \geq T_{\mathrm{f}}$. $H^{\mathrm{mix}}_{\mathrm{frzmlt}} + H^S_{\mathrm{frzmlt}}$ is then returned to CICE as the net potential to grow/melt ice.

TCD
7, 4321–4377, 2013

2.1.5 Representation of the Deep Ocean

We use a three-dimensional grid to represent the deep ocean, with the deep-ocean column at each horizontal (x, y) grid-cell given by

$$T_{\text{ocean}} = \{T(z_1), T(z_2), T(z_3), \ldots T(z_N)\} \tag{19}$$

$$S_{\text{ocean}} = \{S(z_1), S(z_2), S(z_3), \ldots S(z_N)\}, \tag{20}$$

where z represents the vertical ocean grid index and N is the number of vertical levels chosen. At every time-step we assign the mixed layer temperature and salinity to the deep ocean grid within the mixed layer. The signature of Winter Water is therefore retained in the deep ocean as the mixed layer retreats back to a shallower depth. The precise depth levels and T/S data used are described in Sect. 2.2.

The ocean grid is used to determine the temperature and salinity of the waters entrained into the mixed layer, using a linear interpolation scheme to update the value of S_b and T_b to account for the coarse ocean grid. In the case of a very shallow or deep mixed layer we simply set T_b and S_b to top or bottom values. The T/S values for depth levels deeper than the mixed layer at any given time are slowly relaxed back to their initial values to loosely represent ocean dynamics restoring the Winter Water back towards the mean (summertime) ocean conditions. We use a restoration timescale of $R_T = 3$ months as we expect this restoration to take place predominantly through spring.

2.1.6 Ice Dynamics

Since we force the model with near-surface wind speeds, the effect of the turning angle within the atmospheric Ekman layer has been accounted for. However, Kimura (2004) shows the angle between surface winds and ice motion to be around 10–20°, which is a result of the ocean Ekman layer. The ice-ocean drag is given by

$$\tau_{\text{w}} = c_{\text{w}}\rho_{\text{w}}|\boldsymbol{U}_{\text{w}} - \boldsymbol{u}|[(\boldsymbol{U}_{\text{w}} - \boldsymbol{u})\cos\,\theta_{\text{w}} + \mathbf{k} \times (\boldsymbol{U}_{\text{w}} - \boldsymbol{u})\sin\,\theta_{\text{w}}] \tag{21}$$

where $\boldsymbol{u}$ is the ice velocity, $\boldsymbol{U}_w$ is the near-surface ocean velocity (ocean currents are neglected here) and θ_w (= −15° in this study) is the ocean turning angle (negative for the Southern Ocean) between the geostrophic ocean currents and the ocean surface currents under the ice.

2.2 CICE configuration

We have configured CICE to run in stand-alone mode on a 0.5° rotated lat/lon grid (176×176) with the north pole at the equator (i.e. horizontal resolution of around 55 km). An Antarctic landmask and bathymetry are produced through an interpolation of the RTOPO dataset (Timmermann et al., 2010). Atmospheric forcing data are taken from the ERA-Interim reanalysis (Dee et al., 2011) and consist of 6 hourly fields of 10 m zonal and meridional winds, 2 m air temperature and specific humidity, daily fields of downward shortwave and longwave radiation and monthly fields of precipitation (snow and rain). Mean (1980–2011) winter ERA-Interim forcing data are shown in Fig. 2.

We use World Ocean Atlas 09 (WOA09) temperature (Antonov et al., 2010) and salinity (Locarnini et al., 2010) data, which consist of climatological fields of in situ data interpolated to standard depth levels on a 1° grid. These data have been interpolated onto the CICE grid described above, with a weighted extrapolation procedure used to fill any missing grid points found near the coastline, and smoothed using a 9-point gaussian filter. We use a coarse vertical grid to represent the deep ocean, with depth values corresponding to z = (30, 50, 100, 150, 200, 300, 400, 600, 800, 1000) m levels. The WOA09 data at each of these z levels is initialised in our T, S deep ocean grids at each grid point and S_{mix}, T_{mix} and T_S are initialised to the z = 30 m values. The mixed layer salinity is restored back to the monthly climatological (30 m) value with a period of one year, to balance any loss of salt from deep ocean relaxation.

Ice and snow thicknesses are initialised at ∼ 1.5 m and ∼ 0.2 m respectively in the grid cells where the surface temperature is below freezing. We start the model in March when sea ice at its lowest extent (Comiso, 1999, updated 2012) and is approximately the date on which the majority of WOA09 Antarctic shelf sea measurements have been taken (due to this sea ice minimum). The model is spun up for 5 yr (1980–1984), before producing our analysis simulation for 27 yr (1985–2011).

3 Model Results

3.1 Modelled sea ice state

As we are modelling the impact of the atmosphere on the shelf seas, it is important we achieve an accurate sea ice state to validate the fluxes of freshwater, salt, heat and momentum between the atmosphere and the ocean. Figure 4 shows a comparison of the mean (seasonal) modelled ice concentration compared to observations derived from passive microwave emissions using the Bootstrap algorithm (Comiso, 1999, updated 2012). The model does a reasonable job of reproducing the seasonal sea ice cycle, with the best fit to data in autumn (April, May, June), when the mixed layer depth has the highest growth rates. There is, however, an overestimation of the seasonal cycle, with the ice extent too high in winter and too low in summer. The maximum wintertime ice extent is unlikely to be of much importance for our study as we are focused on the impact of sea ice on the southern shelf seas, well away from the wintertime sea ice edge, but the low summer ice concentration is a concern as this extra ice melt will probably over-stratify the shelf seas in summer. In the Weddell Sea, the low ice concentration in summer appears to be linked to low ice concentrations in winter and spring, while in the Amundsen Sea embayment, a polynya forms in spring leading to an ice-free region in summer. The Ross and Bellingshausen seas appear to have the best fit to observations.

Figure 5 shows the mean (seasonal) modelled ice motion. In most regions, the ice follows the pattern of the near-surface winds, with a slight leftward deflection due to the ocean turning angle. There is a strong northward ice motion in the Ross and westward coastal current in East Antarctica as we would expect from both the near surface

TCD
7, 4321–4377, 2013

winds (Fig. 2) and by comparing to ice motion derived from passive microwave feature-tracking (Holland and Kwok, 2012).

Figure 6 shows the mean (seasonal) modelled ice thickness compared to observations of ice thickness from the 2003–2008 ICESat laser altimetry freeboard measurements (Kurtz and Markus, 2012), which assumes that the ice–snow interface is at sea level, i.e. that all freeboard is snow and all draft is solid ice. The modelled results agree well in the general location of regions of thicker and thinner ice, although the absolute values of ice thickness show differences across all seasons and regions. The modelled Weddell Sea ice thickness shows the best fit to observations throughout the year, especially in spring. The model shows a perennially thicker (~ 1 m) sea ice cover in the Bellingshausen Sea which will result in lower growth and melt rates and could also prevent the advection of ice into the Amundsen Sea embayment, where the modelled ice thickness remains very low throughout the year. The model shows perennially thin ice in the Ross Sea, however in spring this is only over the southern half of the shelf sea whereas the observations suggest it could cover a much higher fraction of the shelf sea area.

3.2 Modelled mixed layer

Figure 7a shows the mean (1985–2011) maximum mixed layer depth in each grid cell, demonstrating the ability of this simple mixed layer model to produce the expected pattern of shelf water formation over the Antarctic continental shelf. The mixed layer maximum (which mostly occurs in winter) is deepest in the Weddell and Ross seas, with the black crosses highlighting grid cells where the maximum mixed layer depth is greater than 90% of the water column depth. To further highlight this destratification, Fig. 7b shows the fraction of the water column occupied by the maximum mixed layer depth. Figure 7c shows the mean winter ice thickness, demonstrating a clear relationship between thin ice, high ice production, and deep mixed layers. Figure 8 shows the bottom salinity in summer and winter in the Weddell and Ross shelf seas. The summer minimum salinity fields show the data that the deep ocean is restored towards, while the winter maximum fields show that the model is producing dense waters in sensible areas and with realistic properties.

In the Weddell Sea, Figs. 7a and 8 show a complete destratification along the Ronne Ice Front, over the shallow (∼ 300 m) Berkner Bank in the centre of the shelf and along the Luitpold Coast up to the Brunt Ice Shelf. The summer bottom salinity in Fig. 8 is effectively WOA09 salinity data, due to the relatively rapid (3 month) relaxation time period, showing the highest salinities (∼ 34.8) in the southwest corner of the shelf (reflecting the summertime measurements of Nicholls et al., 2003), fresher waters (∼ 34.6) over the Berkner Bank, near HSSW (∼ 34.7) waters in the Filchner Depression, fresher waters (∼ 34.6) along the Luitpold coast and LSSW (≤ 34.5) near the Brunt Ice Shelf. In winter, complete destratification along the Ronne Ice Front causes the bottom salinity to increase to ∼ 34.9 in a few grid cells, due to the rapid sea ice production (discussed in more detail later). The large region of complete destratification over the shallow Berkner Bank results in little change in salinity, which is still too low to be classified as HSSW, matching well the wintertime observations of this region (Nicholls et al., 2008). Both these results also fit well with the idea discussed by Nicholls et al. (2009), that Modified Warm Deep Water is modified heavily over much of the shelf, mixing with more saline waters formed close to the Ronne Ice Front to give the HSSW signature that is eventually advected off the shelf. Complete destratification along the Luitpold coast has also been observed in recent seal-tag CTD measurements (Årthun et al., 2012), which, in agreement with the model, show a destratified yet low-salinity (∼ 34.4) water column, which is often referred to as Low Salinity Shelf Water (LSSW); salinification is suppressed by fresh Ice Shelf Water present in the region (Fahrbach et al., 1994).

In the Ross Sea, Figs. 7a and 8 show a complete destratification over much of the southern shelf. The summertime bottom salinity in Fig. 8 shows LSSW along the eastern half of the Ross Ice Front and HSSW in the western half, similar to the Weddell shelf and as summarised by Orsi and Wiederwohl (2009). In winter, the water column destratifies along much of the Ross Ice Front and towards the centre of the shelf, also in regions with a shallow water column. Similar to the Weddell Sea, there are only a few regions in which the bottom salinity increases markedly from its summertime value, despite the large region of destratification, with the deep (800–1000 m) water column possibly limiting the potential salinity increase.

Figure 7 shows that the winter maximum mixed layer remains very shallow (< 100 m) in the Bellingshausen Sea, with the deepest (200–300 m) mixed layers found in a small coastal region of Eltanin Bay, where the observations of Tamura et al. (2008) show polynya formation. Deep convection from winter polynyas in Eltanin Bay is discussed in the modelling of study of Holland et al. (2010). Observations of winter mixed layers from thermistor moorings between 2007 and 2010 (Martinson and McKee, 2012) show a mixed layer extending down to around 100–150 m every winter in the Marguerite Bay, while Meredith et al. (2010) find shallower mixed layers further inshore. Observations of the Winter Water depth in summer (Martinson et al., 2008; Jenkins and Jacobs, 2008) show that maximum mixed layer depths are 100–200 m over a much wider area.

The Amundsen Sea in general has deeper maximum mixed layers in winter than the Bellingshausen Sea, with mixed layers in the embayment reaching depths of around 200–300 m and the majority of the remaining shelf sea showing mixed layers reaching depths of 100–200 m. To our knowledge, there are no wintertime oceanographic sections from this region, but summertime observations of Winter Water depth suggest that the mixed layer depth in the embayment, and the deepening tendency towards the coast, are accurate (Jacobs et al., 2011, 2012). However, modelled mixed layer depths near the shelf break are too shallow, and a deepening to the west (Jacobs et al., 2012) is not captured. These features are probably to be driven by Ekman convergence, which is neglected here.

3.3 Analysis of the mixed layer evolution

To understand in more detail the causes of the mixed layer evolution, Fig. 9a–d shows the (2000–2011) deconstructed input of power from the ocean surface to the mixed layer per unit area, from the following: the surface heat flux (including the transfer of latent heat from ice growth and melt) in red; the net salt flux from ice growth and melt in blue; the freshwater flux from evaporation and precipitation in magenta; and wind shearing in green as described in Sect. 2.1.2. Note that these terms are the fraction of power remaining after dissipative effects are taken into account (during deepening only). The evolution of the mean mixed layer depth over the study regions is also shown (in black) to demonstrate how this surface power input drives the mixed layer evolution. Figure 9 shows that in all four regions the net power input (in grey) closely follows the power input from the net salt flux due to ice growth and melt. There is a small contribution from the heat flux term, with wind mixing and precipitation minus evaporation providing a negligible impact.

Figure 9e shows the mean (2000–2011) net surface power input annual cycle for all four regions, highlighting the extremely low autumn/winter mixed layer power input to the Amundsen and Bellingshausen seas compared to the Weddell and Ross seas. This result demonstrates that the deep mixed layers that form in the Weddell and Ross seas can potentially be attributed simply to a greater input of power at the surface in autumn/winter, providing further evidence to support the hypothesis of Talbot (1988) and Petty et al. (2012) that regionally varying surface fluxes can directly explain the bimodal distribution in the shelf seabed temperature. However, the simplicity of our model means that we are not able to rule out a contribution to this distribution from ocean dynamics.

In Fig. 9e we see that the mean Weddell Sea surface power input is roughly symmetric, with no clear winter peak. The Ross Sea mean surface power input has a more pronounced peak in August and a similar inter-annual monthly variability to the Weddell. The Amundsen Sea mean surface power input tends to peak in April, when the mixed layer is shallow, thereby reducing any dissipative effects, while the Bellingshausen Sea shows no real pattern in the peak surface power input across autumn/winter. The mean Ross surface power input is almost double the Weddell throughout autumn/winter, however there is large inter-annual variability in the value of this maximum. The Amundsen and Bellingshausen experience a similar surface power input in July, with a lower surface power input in the Bellingshausen across all other months. The Amundsen and Bellingshausen seas both experience a greater surface power output (removal of power from the mixed layer to the atmosphere) in summer, causing a stronger stratification and further reducing the potential mixed layer deepening in the following winter. This effect is strongest in the Bellingshausen Sea, which has both the lowest power input and largest power output of the four regions.

Figure 9f shows the mean annual energy balance of the mixed layer, calculated through a time integral of the mean power input contributions for each region, with the colours corresponding to the same terms as in Fig. 9a–d. A positive value denotes a net yearly input of energy to the mixed layer, with the deep ocean relaxation removing the excess energy (mainly during spring/summer, representing the advection of more saline waters off the shelf). There is a large input of energy to the WR shelf seas, driven mainly by the salt flux from sea ice growth. The Amundsen shelf sea surface energy input is well balanced, whereas the Bellingshausen shelf sea experiences a net loss of energy due to the large summer freshwater flux from ice melt and also from the freshwater flux due to precipitation. In this case, the loss of energy from the mixed layer must be balanced by diapycnal mixing, represented simply in this model by the relaxation of the mixed layer towards higher salinities.

Figure 9e and f shows the Ross shelf atmosphere provides the greatest input of energy to the ocean, predominantly through the salt flux from ice formation, which may appear to contradict with the observation that the Weddell Sea generates the coldest and most voluminous bottom waters (Gordon et al., 2010). This observation could be explained by either a difference in the waters advecting into the shelf seas that mix with the shelf waters, such as the large flux of freshwater from the Amundsen to the Ross Sea (Assmann and Timmermann, 2005; Jacobs and Giulivi, 2010), or the deeper bathymetry in the Ross Sea along the ice front (Fig. 1), limiting the duration of complete wintertime destratificatiton and thus the rate of salinification. The increase in the flux of fresh glacial melt water from the Amundsen to the Ross Sea has been implicated in the recent Ross sea freshening (Jacobs et al., 2002; Assmann and Timmermann, 2005; Jacobs and Giulivi, 2010), highlighting the additional contribution of this process, which is not explicitly included in this study of surface buoyancy fluxes.

3.4 Regional sea ice mass balance

As we have confirmed sea ice to be the dominant driver of mixed-layer evolution over the Antarctic shelf seas, we now analyse the sea ice mass balance for the four separate regions, to highlight the differences in the growth, melt and export of ice from each region. The difference in ice growth and melt should equal the ice exported out of the region if we assume the ice to be in a regional steady state. The relative contributions to this balance, however, are important as they will influence the mixed layer deepening in winter and freshening in summer. If a large fraction of the ice produced in winter is exported away before it can melt in summer, we would expect deeper mixed layers than in a stable case of ice growth equalling ice melt. Alternatively a net import of ice could provide more ice to melt in summer than was produced the previous winter, providing a fresher summer mixed layer that could inhibit wintertime mixed layer deepening.

The annual ice growth and melt in a specific region (in $m^3\,yr^{-1}$) is calculated as

$$G_i(\text{year}) = \iiint_{R\,\text{year}} \frac{\partial V_i^T}{\partial t}\,\mathrm{d}t\mathrm{d}x\mathrm{d}y \quad \text{where } \frac{\partial V_i^T}{\partial t} > 0 \tag{22}$$

$$M_i(\text{year}) = \iiint_{R\,\text{year}} \frac{\partial V_i^T}{\partial t}\,\mathrm{d}t\mathrm{d}x\mathrm{d}y \quad \text{where } \frac{\partial V_i^T}{\partial t} < 0 \tag{23}$$

where R is the regional shelf sea spatial domain and

$$\frac{\partial V_i^T}{\partial t} = A\frac{\partial h_i^T}{\partial t} + h_i\frac{\partial A^T}{\partial t} \tag{24}$$

where V_i is the volume of ice per unit area (in m) and the superscript T denotes the change in ice state is due to thermodynamic processes only.

The annual ice export out of a specific region (also in $m^3\,yr^{-1}$) is calculated in a similar fashion as

$$E_i(year) = \iint\limits_{R}\int\limits_{year} (\nabla \cdot (\mathbf{u} V_i))\ \mathrm{d}t\mathrm{d}x\mathrm{d}y. \qquad (25)$$

3.4.1 Results from the regional sea ice mass balance

Figure 10 shows the sea ice mass balance of the four study regions, with the results summarised in Table 2. The annual ice growth in Fig. 10a shows that the Weddell ($1020 \pm 112\,km^3$) and Ross ($1280 \pm 92.3\,km^3$) shelf seas grow 2–3 times as much ice each year compared to the Amundsen ($382 \pm 23.0\,km^3$) and Bellingshausen ($481 \pm 43.0\,km^3$) shelf seas. Considering the difference in the size of each shelf sea region, it is also useful to compare this in terms of the mean thickness of ice grown, which normalises the results by the area of each region. The factor of three difference in ice volume growth between the Ross and the Amundsen seas changes to a factor of two when the mean ice thickness growth is considered (2.78 ± 0.20 m and 1.41 ± 0.08 m respectively), due to the relatively small Amundsen shelf sea region. Switching between volume and thickness also changes the region of lowest ice growth, with the lowest mean ice volume growth in the Amundsen, but the lowest mean thickness growth in the Bellingshausen (1.20 ± 0.11 m).

Since we compare these results to studies of polynya ice growth, we also attempt to estimate the ice growth from coastal polynyas. Due to the coarse grid (~ 55 km) we do not expect to be able to fully resolve polynyas, so instead we highlight grid cells with a "high" mean monthly ice growth rate, which we take to be $4\,m\,yr^{-1}$. This value corresponds to the lower end of the Tamura et al. (2008) and Drucker et al. (2011) scales and provides "polynya" grid cells in reasonable locations along the Ross and Ronne ice fronts (Fig. 11). This gives a mean Weddell "polynya" growth of 258 ±

TCD
7, 4321–4377, 2013

34.2 km^3 and a mean Ross mean growth of 578 ± 39.8 km^3. To examine how sea ice growth is distributed within the shelf seas, Fig. 11 shows the mean (1985–2011) annual ice growth. Within the Weddell and Ross shelf seas, the ice growth increases towards the southern coastal ice fronts. The cause of this spatial distribution is investigated in more detail in Sect. 3.5. It is expected that latent heat polynyas form in these coastal regions through the strong northward advection of ice away from the coast. Despite the thin ice in the Ross Sea, it is too thick to be classified as a polynya according to the definition of Martin et al. (2004), who extend the definition of a polynya to include thin ice (< 10–20 cm). Markus et al. (1998) show that the width of the coastal polynyas in the Weddell Sea can be as low as 5 km in winter, considerably less than our grid cell width of ~ 55 km, making it very unlikely that we will simulate either thin ice (< 0.20 m) or a near-zero ice concentration. The Ross Sea polynya is much wider (see Fig. 2 in Drucker et al., 2011), which is why we see more evidence of "polynya" activity along the Ross Ice front in spring. Figure 11 shows the highest modelled mean annual ice growth at around 8 m per year, less than the maximum values found in the observational study of Drucker et al. (2011), which calculates a maximum growth of ~ 15 m yr^{-1} in the Weddell and ~ 28 m yr^{-1} in the Ross, however the larger area the modelled ice growth is calculated over balances the lower area-averaged growth rate.

The precise role and importance of coastal polynyas in shelf-water formation is still under investigation, and a number of recent observational studies have attempted to quantify the ice growth from coastal polynyas in the Weddell Sea (Markus et al., 1998; Renfrew et al., 2002; Drucker et al., 2011), Ross Sea (Martin et al., 2007; Comiso et al., 2011; Drucker et al., 2011) and the entire Antarctic (Tamura et al., 2008). Renfrew et al. (2002) calculate a mean (1992–1998) ice growth in the Ronne Polynya (adjacent to the Ronne Ice Shelf) of 110±30 km^3, similar to the Markus et al. (1998) mean (1992–1994) growth of ~ 87 km^3, the Tamura et al. (2008) mean (1992–2001) growth of 85 ± 25 km^3, and the Drucker et al. (2011) mean (1992–2008) growth of 100 ± 12 km^3. Drucker et al. (2011) also calculate the ice grown in the Eastern Weddell Polynya (EWP) adjacent to the Brunt Ice Shelf, along with a small contribution from a stationary iceberg A23,

TCD
7, 4321–4377, 2013

finding a mean total Weddell polynya ice growth of 240 ± 30 km^3. This compares well to our simulated Weddell polynya growth of 258 ± 34.2 km^3. We can also compare this to our calculated shelf sea ice growth of 1020 ± 112 km^3, with the mean observed Ronne polynya growth therefore accounting for around 10 % of the total ice grown in the model and the total polynya growth from both observations and this study making up around 20 % of the total ice growth. This matches well the salt/heat budget calculation made by Nicholls et al. (2009), who showed that the heat loss from the Ronne Polynya of around 3.5×10^{19} J from the Renfrew et al. (2002) study accounts for only 10 % of the 3×10^{20} J heat loss needed to convert MWDW to HSSW. Including an additional 10 % of the total heat loss from the EWP, the remaining 80 % of ice growth occurs more gradually over the broader shelf sea and is a process lacking in observational analyses. The close fit to this theoretical ratio is an encouraging validation of the model.

In the Ross Sea, Martin et al. (2007) calculate a mean (1992–2002) ice growth in the coastal polynyas (Ross, McMurdo Sound and Terra Nova Bay polynyas) of 500 ± 160 km^3, similar to the Tamura et al. (2008) mean (1992–2001) growth of 450 ± 140 km^3, while Drucker et al. (2011) calculate a higher mean (2003–2008) growth of 740 ± 90 km^3. In all cases the Ross Sea Polynya (RSP) dominates, providing ~ 80–90 % of the total polynya ice growth. The earlier polynya studies are within error of our polynya estimate of 578 ± 39.8 km^3 and comparing these values to our calculated total Ross shelf sea ice growth of 1285 ± 92.3 km^3 shows the Ross polynyas contributing around 30–60 % to the total sea ice growth.

Using this same ice growth calculation procedure, we can estimate the total ice growth of the Weddell (0–60° W) and Ross (135° W–195° W) seas, including over the deep ocean, finding a mean (1985–2011) growth of 4580 ± 278 km^3 in the Weddell and 4564 ± 266 km^3 in the Ross, considerably higher than the 1800 km^3 Weddell ice volume estimate of Renfrew et al. (2002). In our study, the Weddell shelf sea contributes around 20 % to the total Weddell ice growth and the Ross shelf sea contributes around 30 % to the total Ross ice growth.

Comparing the mean annual ice growth map in Fig. 11 with the shelf water formation in Fig. 8, it is clear that high rates of ice growth are not strictly necessary to cause a complete destratification of the water column. In both regions, the formation of shelf water extends further north by several grid points from the coast, with an even larger destratification region over the relatively shallow Berkner Bank in the Weddell, which sees only 1–2 m of ice grown each year. We note, however, that despite the destratification, this does not lead directly to the formation of HSSW but is indirectly important in HSSW formation through the conversion of large volumes of Modified Warm Deep Water to near HSSW. The consistent growth rate along the Ronne Ice Front allows to look at the impact of bathymetry on shelf water formation, as briefly discussed in the previous section, where we see HSSW formation occurring where the water column is at its shallowest (at the southern Berkner Bank). This highlights the potential impact bathymetry can have on HSSW formation, providing further evidence to the claim that the deeper water column along the Ross Ice Front prevents the Ross from producing more HSSW than the Weddell.

Figure 10b shows the annual regional ice melt. The Bellingshausen shelf sea has the highest mean annual melt (0.98 ± 0.16 m) despite having the lowest mean annual ice growth, compared to the Amundsen (0.79 ± 0.13 m), Weddell (0.74 ± 0.14) and Ross (0.44 ± 0.11 m) seas. To our knowledge, there are no observational studies of Antarctic sea ice melt to compare these modelled results to. The high Bellingshausen ice melt is due to the strong import of ice (discussed in more detail in the next paragraph) combined with a warm summertime atmosphere. The Amundsen shelf sea also experiences a relatively warm summer and there is a ready supply of ice to melt through the continuous advection of ice from the Bellingshausen Sea. The Ross Sea rapidly advects ice away from the shelf, reducing the amount of ice available to melt in summer. The Weddell Sea also advects ice northwards but at a slower rate than the Ross, increasing the amount of ice available to melt. Both the Ross and the Weddell shelf seas are forced by a colder atmosphere in summer than the Amundsen and Bellingshausen.

TCD
7, 4321–4377, 2013

The annual regional ice export is shown in Fig. 10c. Note the high inter-annual variability in ice export compared to the other two terms in the sea ice mass balance. There is a large export of ice from the Weddell (1.55 ± 0.54 m) and Ross (2.34 ± 0.33 m) shelf seas and a low export from the Amundsen (0.60 ± 0.43 m) and Bellingshausen (0.26 ± 0.38 m) shelf seas. The ice is advected to the north of the Weddell and Ross shelf seas (shown by the ice motion vectors at the shelf edge in Fig. 10c), driven by strong meridional winds, especially in the Ross, as shown in Fig. 2, removing much of the ice that is grown in winter before it is able to melt in summer (except for a period in the late 1980s where the Weddell export reduces dramatically to near the AB export). Considering the significantly higher meridional wind speed in the Ross, it is perhaps surprising that the difference between the Weddell and Ross export is not greater. An important factor here is the thickness of the ice that is being exported (shown in Fig. 6) with the thicker ice in the Weddell compensating to some degree the reduced meridional ice speed. In contrast, the eastern AB shelf seas show a net import of ice, which is strongest in the eastern Bellingshausen sea, although this is exceeded by a net export of ice to the west of each region. Despite a mean net export of ice out of the Bellingshausen shelf sea, a net import (negative export) is within one standard deviation of the mean. Ice advection between the Bellingshausen and Amundsen seas likely plays an important role in each regional mass balance, however due to the thin width of the connecting shelf sea and the complex coastal geometry of the Amundsen Sea embayment, it is unlikely our model will capture this process accurately, as discussed earlier in Sect. 3.1.

Comparing the modelled ice export with observations in the Weddell, Drucker et al. (2011) calculate a mean (1992–2008) export of 390 ± 130 km^3 (through a straight-line flux-gate centred over the 1000 m deep shelf break) using the motion-tracking area flux estimation of Kwok (2005) combined with an ICESat estimate of Weddell shelf sea ice thickness (0.75 ± 25 m) of Yi et al. (2011). This is the only known estimate of Weddell shelf ice export and is lower than, but within the error of, the 690 ± 243 km^3 value found in this study.

TCD
7, 4321–4377, 2013

Title Page
Abstract Introduction
Conclusions References
Tables Figures
◀ ▶
◀ ▶
Back Close
Full Screen / Esc
Printer-friendly Version
Interactive Discussion

Drucker et al. (2011) calculate a mean (1992–2008) Ross ice export of $700 \pm 350\,\mathrm{km}^3$ using the motion tracking area flux estimation of Kwok (2005) and in-situ Ross shelf sea ice thickness ($0.6 \pm 0.3\,\mathrm{m}$) of Jeffries and Adolphs (1997). This is similar to the Comiso et al. (2011) value of $600 \pm 470\,\mathrm{km}^3$ which used a similar method and dataset. These values are lower than, but within the error of, the $1082 \pm 154\,\mathrm{km}^3$ value found in this study. In both cases, the Kwok (2005) flux-gate used lies to the north of the shelf break in the east, where there is a tendency for ice import, and to the south of the shelf break in the west, where there is a tendency for export. It is therefore expected that the Comiso et al. (2011) and Drucker et al. (2011) estimates are a lower bound of the expected export past the 1000 m isobath contour. The only other known estimate of Ross export is that of Jacobs et al. (2002), which used a simple calculation involving NCEP surface winds and the Jeffries and Adolphs (1997) ice thickness to obtain an estimated export of $1000 \pm 300\,\mathrm{km}^3$, closer to the value found in this study.

There has been little observational analysis of the Amundsen and Bellingshausen shelf sea ice growth and export. Tamura et al. (2008) show that there are potentially small coastal polynyas in the Eltanin Bay in the Bellingshausen Sea, corresponding to our peak region of ice growth in the Bellingshausen shelf sea shown in Fig. 11, and in the Amundsen Sea Embayment, which is not apparent in our study. Assmann and Timmermann (2005) is the only study known to us that has attempted to quantify the ice transport through the Amundsen Sea, using the Bremerhaven Regional Ice Ocean Simulations (BRIOS) model, calculating a mean (1978–2001) annual ice export of $536 \pm 347\,\mathrm{km}^3$. This value is higher than, but within the error of, our calculated export of $163 \pm 118\,\mathrm{km}^3$. The region in Assmann and Timmermann (2005) for which ice export is calculated extends further north of the shelf break, increasing the potential advection of ice to the north.

TCD
7, 4321–4377, 2013

3.5 Linear correlation analysis

To understand the link between spatial and temporal atmospheric variability on the surface-driven deepening of the mixed layer, this section investigates the linear correlation between various atmospheric variables and the net surface power input to the mixed layer in autumn/winter (April–September). Specifically, Table 3 demonstrates the spatial correlation between the mean (1985–2011) autumn/winter atmospheric forcing and the mean (1985–2011) autumn/winter surface power input, with one point used for each grid cell within the regions shown in Fig. 9. Figure 12 demonstrates the temporal correlation between the shelf-sea mean autumn/winter atmospheric forcing to the shelf-sea mean autumn/winter net surface power input, with one point used for each year for each region. This regression is shown graphically to demonstrate the variability in the mean atmospheric forcing over each of the shelf seas. The potential for summer stratification preconditioning the following winter mixed layer deepening has been discussed previously (e.g. by Meredith et al., 2004, for the Bellingshausen Sea) and so it is included as a further variable in both studies. All variables are regressed against the mean net surface power input in autumn/winter (April–September) as this represents both the mixed layer deepening and potential salinification of the mixed layer. Note that in the following discussion, we take $r^2 < 0.2$ to imply weak correlation, an r^2 of 0.2–0.5 to imply moderate correlation, and an $r^2 > 0.5$ to imply strong correlation. Correlations discussed are significant at 99 % unless otherwise stated (correlations < 99 % are also listed in the table/figure).

Considering the significant intra-regional spatial correlations (r^2 values) listed in Table 3, the temporal mean Weddell autumn/winter net surface power input shows strong spatial correlation to the summer (January–March) net surface power input (0.55), moderate correlation to incoming shortwave radiation (0.43), specific humidity (0.30) and air temperature (0.24), and weak correlation to the zonal wind speed (0.18) and meridional wind speed (0.07). The Bellingshausen autumn/winter net surface power input shows moderate correlation to the meridional wind speed (0.33), air temperature

TCD
7, 4321–4377, 2013

(0.27), incoming longwave radiation (0.25), specific humidity (0.23), and weak correlation to the incoming shortwave radiation (0.18) and zonal wind speed (0.18). The Amundsen autumn/winter net surface power input shows moderate correlation to the summer net surface power input (0.26), and weak correlation to the specific humidity (0.14), air temperature (0.14), incoming longwave radiation (0.14) and incoming shortwave radiation (0.13). The Ross autumn/winter net surface power input shows very strong correlation to the summer (January–March) net surface power input (0.81) and air temperature (0.54), and moderate correlation to specific humidity (0.44) and incoming shortwave radiation (0.36), and weak correlation to precipitation (0.09) and zonal wind speed (0.08).

It was expected that the air temperature would show a strong spatial correlation to the autumn/winter net surface power input, based on the study of Petty et al. (2012) which demonstrated the large impact of air temperature on mixed layer depth variability. However, the more sophisticated 2-D ice dynamics of CICE complicates the results of the simple sea ice model by advecting ice into neighbouring grid cells, affecting their resultant thermodynamic behaviour. A combination of low air temperatures, high ice growth and strong net export of ice out of a grid cell should lead to a consistently greater winter destratification, i.e. the process taking place along the coastal ice fronts, where ice is only advected northwards without any import of ice from the south. The perennially thin ice cover in the Ross Sea probably explains the greater correlation between intra-regional atmospheric variability and the net surface power input, with the thicker ice present in the other shelf seas insulating them against any intra-regional atmospheric variability. The lack of strong spatial correlation with the winds is unsurprising, as it is the ice divergence that plays the crucial role locally, where we expect the divergence to be at a maximum near the coast, which might not necessarily correspond to regions of stronger winds. The high ice growth rates near to the coast and the continuous export of ice to the north in the Weddell and Ross Seas (as described earlier in Sect. 3.4.1) will lead to a greater autumn/winter net surface power input and will reduce the availability of ice to melt in summer. This could also explain the strong correlation

TCD
7, 4321–4377, 2013

between the summer net surface power input and autumn/winter surface power input as opposed to the causative impact of less summer melt and therefore a less stratified summer water column on the subsequent mixed layer deepening, however this could also be an additional positive feedback.

Considering the significant spatial (shelf-sea) mean temporal correlations (r^2 values) shown in Fig. 12, the spatial mean Weddell autumn/winter net surface power input shows strong temporal correlation to the meridional wind speed (0.59), moderate correlation to the summer net surface power input (0.35), specific humidity (0.34), incoming longwave radiation (0.35), precipitation (0.30) and air temperature (0.28), and weak correlation to the zonal wind speed (0.18, 97.3 %). The mean Bellingshausen autumn/winter net surface power input shows strong correlation to the incoming longwave radiation (0.68), air temperature (0.66), precipitation (0.64), specific humidity (0.63) and meridional wind speed (0.60). The mean Amundsen autumn/winter power input shows strong correlation to the meridional wind speed (0.77), air temperature (0.76), incoming longwave radiation (0.71) and specific humidity (0.70), and moderate correlation to precipitation (0.49), and weak correlation to the incoming shortwave radiation (0.16, 95.8 %) and summer net surface power input (0.15, 95.4 %). The mean Ross autumn/winter net surface power input shows moderate correlation to the zonal wind speed (0.47), precipitation (0.39), incoming shortwave radiation (0.38) and incoming longwave radiation (0.37), and a weak correlation to the specific humidity (0.26), air temperature (0.24) and summer net surface power input (0.22, 98.7 %). Note that all variables in this temporal correlation show less variance than in the spatial correlations described above (i.e. atmospheric and summer power input show greater spatial variance within each shelf sea compared to the mean shelf sea temporal variability).

The mean shelf sea autumn/winter net surface power input shows a strong temporal correlation to most of the thermodynamic forcing variables in the Bellingshausen and Amundsen shelf seas, especially for air temperature, specific humidity, incoming longwave radiation and precipitation, which are all strongly coupled through cloud formation. The weaker correlation to these variables in the Weddell and Ross may be

Discussion Paper | Discussion Paper | Discussion Paper | Discussion Paper |

TCD
7, 4321–4377, 2013

due to ocean feedbacks as a result of deeper mixed layers such as an enhanced ocean heat flux, or the weaker correlation between the atmospheric variables due to stronger winds. The strong correlation to meridional winds compared to zonal winds in the Amundsen and Bellingshausen can be explained by the mean ice motion and geometry of the regions (Fig. 5). Only a more northward (positive) meridional wind anomaly could increase divergence, as a more westward (negative) zonal flow would simply increase both the import of ice from the east and export to the west of each region.

An interesting result is the lack of correlation between the net surface power input and the meridional wind speed in the Ross. Intuitively we might expect that stronger meridional winds would lead to greater net ice divergence and thus increased ice production, as we see in the Weddell. Figure 13 shows the correlations of further temporal linear regressions that were carried out to investigate this in more detail. Figure 13a shows the correlation between the annual Ross ice export (E_i) and the spatial mean autumn/winter zonal and meridional wind speed, demonstrating a moderate correlation between the ice export and the zonal wind speed (0.28), but no correlation to the meridional wind speed. Figure 13b then shows a moderate anti-correlation (0.27) between the autumn/winter meridional and zonal wind speeds. These results are thought to be due to the location of the Ross Sea pressure low (as discussed in more detail by Comiso et al., 2011), where specific locations of the low change the orientation of the isobars across the shelf, meaning greater meridional winds thus appear to reduce the zonal component of the wind (less eastward) and vice versa. Cape Adare in the east of the Ross shelf sea appears to hinder the export of ice out of the shelf, as demonstrated by the thick ice produced along the coast here (Fig. 6). A more eastward wind direction will result in ice being advected more perpendicular to both the ice front and shelf break, away from the Cape Adare coast, potentially increasing ice export. The ocean turning angle (Eq. 21) probably plays an important role here due to the leftward deflection of the ice motion in response to the predominantly meridional winds (see Figs. 2 and 5). The mean zonal wind speed shows greater variance than the meridional winds, making the process described more likely to generate an observable difference in ice export compared to changes in the meridional winds. Another complicating factor in this discussion is the impact of ice thickness on the resultant link between winds and export, which was highlighted by Comiso et al. (2011) as a key area of uncertainty in such discussions.

4 Conclusions

A prognostic mixed layer model has been incorporated into the Los Alamos sea ice model CICE, to investigate the cause of regional variations in the formation of Antarctic shelf sea waters. This model captures reasonably well the expected ice concentration and sea ice thickness distribution through comparison to observations and produces deep (> 500 m) mixed layers in the Weddell and Ross shelf seas each winter as expected. This results in the complete destratification of the water column along the southern coastal ice fronts in both seas, leading to High Salinity Shelf Water (HSSW) formation. The water column is also destratified in shallow regions further north (e.g. the Berkner Bank in the central Weddell shelf) which do not lead to HSSW formation but do provide an important mechanism through which Modified Warm Deep Water (MWDW) is converted to near HSSW. Shallow mixed layers form in the Amundsen (∼ 200 m) and Bellingshausen (< 100 m) shelf seas.

By deconstructing the surface power input to the mixed layer, we find that the salt flux from sea ice growth/melt dominates the evolution of the mixed layer in all regions, with a smaller contribution from the surface heat flux. The Weddell and Ross shelf seas receive a net input of energy at the surface (mainly through the autumn/winter salt flux), which is used to convert MWDW to HSSW, with the excess energy removed each year through deep-ocean restoring, which represents ocean dynamics neglected by this model. The Amundsen shelf sea is well-balanced, with the surface input of energy in autumn/winter balanced by the loss of energy from surface forcing in spring/summer.

The Bellingshausen shelf sea experiences an annual surface energy deficit, due primarily to a strong freshwater flux in spring/summer.

An analysis of the sea ice mass balance demonstrates the contrasting growth, melt and export of ice in each region. The Ross shelf sea has the highest mean annual ice growth, followed by the Weddell shelf sea, with the two regions growing two/three times as much ice as the Amundsen and Bellingshausen shelf seas. Despite this, the Bellingshausen shelf sea has the highest mean annual ice melt of the shelf seas, driven in large part by the warm summer atmosphere and continuous ice import from the north-east, which explains the strong summer stratification and shallow mixed layers that form here in winter. In contrast, a large fraction of the ice that is grown over the Weddell and Ross shelves is exported to the north each year ($\gtrsim$40 % and $\gtrsim$70 % respectively). These results compare well to the estimated ice growth needed for MWDW-HSSW conversion in the Weddell Sea calculated by Nicholls et al. (2009), and both the Weddell and Ross export estimates lie within the range calculated by Drucker et al. (2011). Comparing our modelled ice growth estimates to polynya ice growth observations suggest the coastal polynyas contribute ~ 20 % to Weddell shelf sea ice growth and ~ 30–60 % to the Ross shelf sea ice growth. Sea ice growth outside the Ross and Weddell coastal polynyas is therefore expected to be an important shelf sea process that currently lacks observational analysis.

A linear regression analysis is performed to determine the temporal and spatial correlations between the autumn/winter mixed layer power input and several atmospheric variables. The Weddell and Ross temporal mean autumn/winter power input shows strong spatial correlation to the summer power input and moderate correlation to the autumn/winter air temperature, specific humidity and incoming shortwave radiation. The Bellingshausen temporal mean autumn/winter power input shows moderate spatial correlation to the autumn/winter air temperature, specific humidity, incoming shortwave, incoming longwave and the meridional wind speed. The Amundsen temporal mean autumn/winter power input only shows a moderate correlation to the summer power input. The Amundsen and Bellingshausen spatial (shelf-sea) mean autumn/winter power input shows strong temporal correlation to the autumn/winter air temperature, specific humidity, incoming longwave radiation and precipitation. The Weddell and Ross spatial (shelf-sea) mean autumn/winter power input show only a moderate correlation to the same atmospheric variables. All regions show strong temporal correlation between the spatial (shelf-sea) mean autumn/winter surface power input and the meridional wind speed except the Ross, which instead shows moderate correlation to the zonal wind speed. Further regressions demonstrate that this may be due to the Ross shelf-sea geometry and impact of the ocean turning angle on ice motion, with a more zonal wind preventing ice build up along the Cape Adare coast in the eastern Ross shelf sea.

Acknowledgements. We would like to thank D. Schroeder for assistance in the initial CICE configuration and in acquiring and re-gridding the atmospheric forcing sets used in this study.

References

Antonov, J. I., Seidov, D., Boyer, T. P., Locarnini, R. A., Mishonov, A. V., Garcia, H. E., Baranova, O. K., Zweng, M. M., and Johnson, D. R.: World Ocean Atlas 2009, vol. 2: Salinity, edited by: Levitus, S.,. NOAA Atlas NESDIS, 69, 184 pp., 2010. 4334, 4365

Arneborg, L., Wahlin, A. K., Bjork, G., Liljebladh, B., and Orsi, A. H.: Persistent inflow of warm water onto the central Amundsen shelf, Nat. Geosci., 5, 876–880, doi:10.1038/ngeo1644, 2012. 4325

Årthun, M., Nicholls, K. W., and Boehme, L.: Wintertime water mass modification near an Antarctic ice front, J. Phys. Oceanogr., 43, 359–365, doi:10.1175/JPO-D-12-0186.1, 2012. 4337

Assmann, K. and Timmermann, R.: Variability of dense water formation in the Ross Sea, Ocean Dynam., 55, 68–87, doi:10.1007/s10236-004-0106-7, 2005. 4325, 4340, 4347

Assmann, K. M., Hellmer, H. H., and Jacobs, S. S.: Amundsen Sea ice production and transport, J. Geophys. Res., 110, C12013, doi:10.1029/2004JC002797, 2005. 4325

Bitz, C. M. and Lipscomb, W. H.: An energy-conserving thermodynamic model of sea ice, J. Geophys. Res., 104, 15669–15677, doi:10.1029/1999JC900100, 1999. 4326

TCD
7, 4321–4377, 2013

Comiso, J.: Bootstrap Sea Ice Concentrations from Nimbus-7 SMMR and DMSP SSM/I-SSMIS, National Snow and Ice Data Center, Boulder, Colorado USA, 1999, updated 2012. 4334, 4335, 4368

Comiso, J. C., Kwok, R., Martin, S., and Gordon, A. L.: Variability and trends in sea ice extent and ice production in the Ross Sea, J. Geophys. Res., 116, C04021, doi:10.1029/2010JC006391, 2011. 4343, 4347, 4351, 4352

de Steur, L., Holland, D., Muench, R., and McPhee, M.: The warm-water halo around Maud Rise: properties, dynamics and impacts, Deep-Sea Res. Pt. I, 54, 871–896, doi:10.1016/j.dsr.2007.03.009, 2007. 4330

Dee, D. P., Uppala, S. M., Simmons, A. J., Berrisford, P., Poli, P., Kobayashi, S., Andrae, U., Balmaseda, M. A., Balsamo, G., Bauer, P., Bechtold, P., Beljaars, A. C. M., van de Berg, L., Bidlot, J., Bormann, N., Delsol, C., Dragani, R., Fuentes, M., Geer, A. J., Haimberger, L., Healy, S. B., Hersbach, H., Hólm, E. V., Isaksen, L., Kållberg, P., Köhler, M., Matricardi, M., McNally, A. P., Monge-Sanz, B. M., Morcrette, J.-J., Park, B.-K., Peubey, C., de Rosnay, P., Tavolato, C., Thépaut, J.-N., and Vitart, F.: The ERA-interim reanalysis: configuration and performance of the data assimilation system, Q. J. Roy. Meteor. Soc., 137, 553–597, doi:10.1002/qj.828, 2011. 4334, 4366

Drucker, R., Martin, S., and Kwok, R.: Sea ice production and export from coastal polynyas in the Weddell and Ross Seas, Geophys. Res. Lett., 38, L17502, doi:10.1029/2011GL048668, 2011. 4324, 4342, 4343, 4344, 4346, 4347, 4353

Fahrbach, E., Peterson, R., Rohardt, G., Schlosser, P., and Bayer, R.: Suppression of bottom water formation in the southeastern Weddell sea, Deep-Sea Res. Pt. I, 41, 389–411, 1994. 4337

Foldvik, A., Gammelsrød, T., Østerhus, S., Fahrbach, E., Rohardt, G., Schroder, M., Nicholls, K. W., Padman, L., and Woodgate, R. A.: Ice shelf water overflow and bottom water formation in the southern Weddell Sea, J. Geophys. Res., 109, C02015, doi:10.1029/2003JC002008, 2004. 4324

Foster, T. D. and Carmack, E. C.: Frontal zone mixing and Antarctic Bottom water formation in the southern Weddell Sea, Deep-Sea Res. Ocean., 23, 301–317, 1976. 4323

Fricker, H. A. and Padman, L.: Thirty years of elevation change on Antarctic Peninsula ice shelves from multimission satellite radar altimetry, J. Geophys. Res., 117, C02026, doi:10.1029/2011JC007126, 2012. 4323, 4325

Gill, A. E.: Circulation and bottom water production in the Weddell Sea, Deep-Sea Res. Ocean., 20, 111–140, 1973. 4323
Gordon, A. L., Huber, B. A., Hellmer, H. H., and Ffield, A.: Deep and bottom water of the Weddell Sea's western rim, Science, 262, 95–97, 1993. 4323
Gordon, A. L., Huber, B., McKee, D., and Visbeck, M.: A seasonal cycle in the export of bottom water from the Weddell Sea, Nat. Geosci., 3, 551–556, 2010. 4340
Hibler, W. D.: A dynamic thermodynamic sea ice model, J. Phys. Oceanogr., 9, 815–846, 1979. 4326
Holland, P. R. and Kwok, R.: Wind-driven trends in Antarctic sea-ice drift, Nat. Geosci., 5, 872–875, doi:10.1038/ngeo1627, 2012. 4336
Holland, P. R., Jenkins, A., and Holland, D. M.: Ice and ocean processes in the Bellingshausen Sea, Antarctica, J. Geophys. Res., 115, C0502, doi:10.1029/2008JC005219, 2010. 4323, 4325, 4338
Hunke, E. C. and Dukowicz, J. K.: An elastic viscous plastic model for sea ice dynamics, J. Phys. Oceanogr., 27, 1849–1867, 1997. 4326
Hunke, E. C. and Lipscomb, W. H.: CICE: the Los Alamos Sea Ice Model Documentation and Software Users Manual Version 4.0 LA-CC-06-012, 2008. 4326
Jacobs, S. S.: Bottom water production and its links with the thermohaline circulation, Antarct. Sci., 16, 427–437, doi:10.1017/S095410200400224X, 2004. 4323, 4324
Jacobs, S. S. and Giulivi, C. F.: Large multidecadal salinity trends near the Pacific–Antarctic continental margin, J. Climate, 23, 4508–4524, doi:10.1175/2010JCLI3284.1, 2010. 4340, 4341
Jacobs, S. S., Amos, A. F., and Bruchhausen, P. M.: Ross Sea oceanography and Antarctic Bottom Water formation, Deep-Sea Res. Ocean., 17, 935–962, 1970. 4323, 4324
Jacobs, S. S., Fairbanks, R. G., and Horibe, Y. G.: Origin and evolution of water masses near the Antarctic continental margin: evidence from $H_2^{18}O/H_2^{16}O$ ratios in seawater, Antarct. Res. Ser., 43, 59–85, doi:10.1029/AR043p0059, 1985. 4324
Jacobs, S. S., Hellmer, H. H., and Jenkins, A.: Antarctic Ice Sheet melting in the Southeast Pacific, Geophys. Res. Lett., 23, 957–960, doi:10.1029/96GL00723, 1996. 4323
Jacobs, S. S., Giulivi, C. F., and Mele, P. A.: Freshening of the Ross Sea during the late 20th century, Science, 297, 386–389, doi:10.1126/science.1069574, 2002. 4340, 4347

TCD
7, 4321–4377, 2013

Antarctic sea ice and mixed layer

A. A. Petty et al.

Jacobs, S. S., Jenkins, A., Giulivi, C. F., and Dutrieux, P.: Stronger ocean circulation and increased melting under Pine Island Glacier ice shelf, Nat. Geosci., 4, 519–523, doi:10.1038/ngeo1188, 2011. 4323, 4325, 4338

Jacobs, S. S., Jenkins, A., Hellmer, H., Giulivi, C., Nitsche, F., Huber, B., and Guerrero, R.: The Amundsen Sea and the Antarctic Ice Sheet, Oceanography, 25, 154–163, doi:10.5670/oceanog.2012.90, 2012. 4338

Jeffries, M. O. and Adolphs, U.: Early winter ice and snow thickness distribution, ice structure and development of the western Ross Sea pack ice between the ice edge and the Ross Ice Shelf, Antarct. Sci., 9, 188–200, 1997. 4347

Jenkins, A. and Jacobs, S.: Circulation and melting beneath George VI Ice Shelf, Antarctica, J. Geophys. Res., 113, C04013, doi:10.1029/2007JC004449, 2008. 4323, 4338

Johnson, G. C.: Quantifying Antarctic bottom water and North Atlantic deep water volumes, J. Geophys. Res., 113, C05027, doi:10.1029/2007JC004477, 2008. 4324

Kim, J.-W.: A generalized bulk model of the oceanic mixed layer, J. Phys. Oceanogr., 6, 686–695, 1976. 4362

Kimura, N.: Sea ice motion in response to surface wind and ocean current in the southern ocean, J. Meteorol. Soc. Jpn. II, 82, 1223–1231, 2004. 4333

Klinck, J., Hofmann, E., Beardsley, R., Salihoglu, B., and Howard, S.: Water-mass properties and circulation on the west Antarctic Peninsula Continental Shelf in Austral Fall and Winter 2001, Deep-Sea Res. Pt. II, 51, 1925–1946, doi:10.1016/j.dsr2.2004.08.001, 2004. 4325

Kraus, E. B. and Turner, J. S.: A one-dimensional model of the seasonal thermocline, II. The general theory and its consequences, Tellus, 19, 98–106, doi:10.1111/j.2153-3490.1967.tb01462.x, 1967. 4326, 4330

Kurtz, N. T. and Markus, T.: Satellite observations of Antarctic sea ice thickness and volume, J. Geophys. Res., 117, C08025, doi:10.1029/2012JC008141, 2012. 4336, 4370

Kwok, R.: Ross Sea ice motion, area flux, and deformation, J. Climate, 18, 3759–3776, doi:10.1175/JCLI3507.1, 2005. 4346, 4347

Lemke, P. and Manley, T. O.: The seasonal variation of the mixed layer and the pycnocline under polar sea ice, J. Geophys. Res., 89, 6494–6504, doi:10.1029/JC089iC04p06494, 1984. 4362

Lemke, P., Owens, W. B., and Hibler, W. D.: A coupled sea ice-mixed layer-pycnocline model for the Weddell Sea, J. Geophys. Res., 95, 9513–9525, doi:10.1029/JC095iC06p09513, 1990. 4330

TCD

7, 4321–4377, 2013

Lindsay, R. W., Holland, D. M., and Woodgate, R. A.: Halo of low ice concentration observed over the Maud Rise seamount, Geophys. Res. Lett., 31, L13302, doi:10.1029/2004GL019831, 2004. 4330
Locarnini, R. A., Mishonov, A. V., Antonov, J. I., Boyer, T. P., Garcia, H. E., Baranova, O. K., Zweng, M. M., and Johnson, D. R.: World Ocean Atlas 2009, vol. 1: Temperatures, edited by: Levitus, S., NOAA Atlas NESDIS 68, 1, 2010. 4334, 4365
Markus, T., Kottmeier, C., and Fahrbach, E.: Ice formation in coastal polynyas in the Weddell Sea and their impact on oceanic salinity, in: Antarctic Sea Ice: Physical Processes, Interactions and Variability, American Geophysical Union, doi:10.1029/AR074p0273, 273–292, 1998. 4343
Martin, S., Drucker, R., Kwok, R., and Holt, B.: Estimation of the thin ice thickness and heat flux for the Chukchi Sea Alaskan coast polynya from special sensor microwave/imager data, 1990–2001, J. Geophys. Res., 109, C10012, doi:10.1029/2004JC002428, 2004. 4343
Martin, S., Drucker, R. S., and Kwok, R.: The areas and ice production of the western and central Ross Sea polynyas, 1992–2002, and their relation to the B-15 and C-19 iceberg events of 2000 and 2002, J. Marine Syst., 68, 201–214, available at: http://www.sciencedirect.com/science/article/pii/S09247963060%03502, 2007. 4343, 4344
Martinson, D. G., Stammerjohn, S. E., Iannuzzi, R. A., Smith, R. C., and Vernet, M.: Western Antarctic Peninsula physical oceanography and spatio-temporal variability, Deep Sea Research Part II: Topical Studies in Oceanography, 55, 1964–1987, doi:10.1016/j.dsr2.2008.04.038, 2008. 4323, 4338
Martinson, D. G. and McKee, D. C.: Transport of warm upper circumpolar deep water onto the western Antarctic Peninsula continental shelf, Ocean Sci., 8, 433–442, doi:10.5194/os-8-433-2012, 2012. 4325, 4338
Maykut, G. A. and Untersteiner, N.: Some results from a time-dependent thermodynamic model of sea ice, J. Geophys. Res., 76, 1550–1575, doi:10.1029/JC076i006p01550, 1971. 4326
Meredith, M. P., Renfrew, I. A., Clarke, A., King, J. C., and Brandon, M. A.: Impact of the 1997/98 ENSO on upper ocean characteristics in Marguerite Bay, western Antarctic Peninsula, J. Geophys. Res., 109, C09013–, doi:10.1029/2003JC001784, 2004. 4325, 4348
Meredith, M. P., Wallace, M. I., Stammerjohn, S. E., Renfrew, I. A., Clarke, A., Venables, H. J., Shoosmith, D. R., Souster, T., and Leng, M. J.: Changes in the freshwater composition of the upper ocean west of the Antarctic Peninsula during the first decade of the 21st century, Prog. Oceanogr., 87, 127–143, doi:10.5194/os-8-433-2012, 2010. 4338

Nicholls, K. W., Padman, L., Schröder, M., Woodgate, R. A., Jenkins, A., and Østerhus, S.: Water mass modification over the continental shelf north of Ronne Ice Shelf, Antarctica, J. Geophys. Res., 108, 3260, doi:10.1029/2002JC001713, 2003. 4337

Nicholls, K. W., Boehme, L., Biuw, M., and Fedak, M. A.: Wintertime ocean conditions over the southern Weddell Sea continental shelf, Antarctica, Geophys. Res. Lett., 35, L21605, doi:10.1029/2008GL035742, 2008. 4337

Nicholls, K. W., Østerhus, S., Makinson, K., Gammelsrød, T., and Fahrbach, E.: Ice-ocean processes over the continental shelf of the southern Weddell Sea, Antarctica: a review, Rev. Geophys., 47, RG3003, doi:10.1029/2007RG000250, 2009. 4323, 4324, 4337, 4344, 4353

Niiler, P. and Kraus, E. B.: One-dimensional models of the upper ocean, in: Modeling and Prediction of the Upper Layers of the Ocean, 143–172, 1977. 4326, 4330

Ohshima, K. I., Fukamachi, Y., Williams, G. D., Nihashi, S., Roquet, F., Kitade, Y., Tamura, T., Hirano, D., Herraiz-Borreguero, L., Field, I., Hindell, M., Aoki, S., and Wakatsuchi, M.: Antarctic bottom water production by intense sea-ice formation in the Cape Darnley polynya, Nat. Geosci., advance online publication, doi:10.1038/ngeo1738, 2013. 4324

Orsi, A., Johnson, G., and Bullister, J.: Circulation, mixing, and production of Antarctic Bottom Water, Prog. Oceanogr., 43, 55–109, 1999. 4323, 4324

Orsi, A. H. and Wiederwohl, C. L.: A recount of Ross Sea waters, Deep-Sea Res. II, 56, 778–795, doi:10.1016/j.dsr2.2008.10.033, 2009. 4323, 4337

Orsi, A. H., Jacobs, S. S., Gordon, A. L., and Visbeck, M.: Cooling and ventilating the Abyssal Ocean, Geophys. Res. Lett., 28, 2923–2926, doi:10.1029/2001GL012830, 2001. 4323

Petty, A. A., Feltham, D. L., and Holland, P. R.: Impact of atmospheric forcing on Antarctic continental shelf water masses, J. Phys. Oceanogr., 43, 920–940, doi:10.1175/JPO-D-12-0172.1, 2012. 4325, 4326, 4327, 4330, 4339, 4349

Pritchard, H. D., Ligtenberg, S. R. M., Fricker, H. A., Vaughan, D. G., van den Broeke, M. R., and Padman, L.: Antarctic ice-sheet loss driven by basal melting of ice shelves, Nature, 484, 502–505, doi:10.1038/nature10968, 2012. 4323, 4325

Renfrew, I. A., King, J. C., and Markus, T.: Coastal polynyas in the southern Weddell Sea: variability of the surface energy budget, J. Geophys. Res., 107, 3063, doi:10.1029/2000JC000720, 2002. 4324, 4343, 4344

Rignot, E., Jacobs, S., Mouginot, J., and Scheuchl, B.: Ice shelf melting around Antarctica, Science, 341, 266–270, doi:10.1126/science.1235798, 2013. 4323, 4325

Shepherd, A., Wingham, D., and Rignot, E.: Warm ocean is eroding West Antarctic Ice Sheet, Geophys. Res. Lett., 31, L23402, doi:10.1029/2004GL021106, 2004. 4323, 4325

Talbot, M. H.: Oceanic environment of George VI Ice Shelf, Antarctic Peninsula, Ann. Glaciol., 11, 161–164, 1988. 4323, 4339

Tamura, T., Ohshima, K. I., and Nihashi, S.: Mapping of sea ice production for Antarctic coastal polynyas, Geophys. Res. Lett., 35, L07606, doi:10.1029/2007GL032903, 2008. 4338, 4342, 4343, 4344, 4347

Thoma, M., Jenkins, A., Holland, D., and Jacobs, S.: Modelling circumpolar deep water intrusions on the Amundsen Sea continental shelf, Antarctica, Geophys. Res. Lett., 35, L18602, doi:10.1029/2008GL034939, 2008. 4325

Timmermann, R., Beckmann, A., and Hellmer, H. H.: Simulations of ice-ocean dynamics in the Weddell Sea, 1. Model configuration and validation, J. Geophys. Res., 107, 3024, doi:10.1029/2000JC000741, 2002. 4325

Timmermann, R., Le Brocq, A., Deen, T., Domack, E., Dutrieux, P., Galton-Fenzi, B., Hellmer, H., Humbert, A., Jansen, D., Jenkins, A., Lambrecht, A., Makinson, K., Niederjasper, F., Nitsche, F., Nøst, O. A., Smedsrud, L. H., and Smith, W. H. F.: A consistent data set of Antarctic ice sheet topography, cavity geometry, and global bathymetry, Earth Syst. Sci. Data, 2, 261–273, doi:10.5194/essd-2-261-2010, 2010. 4334, 4365

van Lipzig, N. P. M., Turner, J., Colwell, S. R., and van Den Broeke, M. R.: The near-surface wind field over the Antarctic continent, Int. J. Climatol., 24, 1973–1982, doi:10.1002/joc.1090, 2004. 4324

Wåhlin, A. K., Yuan, X., Björk, G., and Nohr, C.: Inflow of Warm Circumpolar Deep Water in the Central Amundsen Shelf, J. Phys. Oceanogr., 40, 1427–1434, doi:10.1175/2010JPO4431.1, 2010. 4325

Walker, D. P., Brandon, M. A., Jenkins, A., Allen, J. T., Dowdeswell, J. A., and Evans, J.: Oceanic heat transport onto the Amundsen Sea shelf through a submarine glacial trough, Geophys. Res. Lett., 34, L02602, doi:10.1029/2006GL028154, 2007. 4325

Wilchinsky, A. V. and Feltham, D. L.: Numerical simulation of the Filchner overflow, J. Geophys. Res., 114, C12012, doi:10.1029/2008JC005013, 2009. 4324

Williams, G. D., Aoki, S., Jacobs, S. S., Rintoul, S. R., Tamura, T., and Bindoff, N. L.: Antarctic bottom water from the Adélie and George V land coast, East Antarctica (140–149° E), J. Geophys. Res., 115, C04027, doi:10.1029/2009JC005812, 2010. 4324

Yi, D., Zwally, H. J., and Robbins, J. W.: ICESat observations of seasonal and interannual variations of sea-ice freeboard and estimated thickness in the Weddell Sea, Antarctica (2003–2009), Ann. Glaciol., 52, 43–51, doi:10.3189/172756411795931480, 2011. 4346

Table 1. Constants and parameters referred to in the model description

	Constants
α	thermal expansion coefficient, $5.82 \times 10^{-5}\,\mathrm{K^{-1}}$
β	saline contraction coefficient, 8×10^{-4}
c_p	specific heat capacity of water, $4190\,\mathrm{J\,kg^{-1}\,K^{-1}}$
g	acceleration due to gravity, $9.81\,\mathrm{m\,s^{-2}}$
L_v	latent heat of vaporisation, $2.501 \times 10^{6}\,\mathrm{J\,kg^{-1}}$
ρ_w	density of water, $1026\,\mathrm{kg\,m^{-3}}$
ρ_i	density of ice, $930\,\mathrm{kg\,m^{-3}}$
	Fixed Parameters
c_m	unsteadiness coefficient, $0.03\,\mathrm{m\,s^{-1}}$(Kim, 1976)
d_B	scale depth of convective dissipation, 50 m(Lemke and Manley, 1984)
d_w	scale depth of mechanical dissipation, 10 m(Lemke and Manley, 1984)
Δz	ocean profile vertical resolution, 0.5 m
h_min	minimum mixed layer depth, 20 m
h_S	surface (temperature) layer thickness, 10 m

Discussion Paper | Discussion Paper | Discussion Paper | Discussion Paper |

TCD

7, 4321–4377, 2013

Antarctic sea ice and mixed layer

A. A. Petty et al.

Table 2. Regional sea ice mass balance contributions, taken from Fig. 10. The errors shown correspond to one standard deviation in the inter annual variability.

	Weddell	Bellingshausen	Amundsen	Ross
Shelf sea area (10^3 km^2)	445	398	271	462
"Polynya" area (10^3 km^2)	52.0	–	–	96.8
Mean ice growth (m yr^{-1})	2.29 ± 0.25	1.20 ± 0.11	1.41 ± 0.08	2.78 ± 0.20
Mean ice growth (km^3 yr^{-1})	1020 ± 112	481 ± 43.0	382 ± 23.0	1285 ± 92.3
"Polynya" contribution (m yr^{-1})	4.96 ± 0.67	–	–	5.98 ± 0.41
"Polynya" contribution (km^3 yr^{-1})	257.8 ± 34.2	–	–	578.4 ± 39.8
Mean ice melt (m yr^{-1})	0.74 ± 0.14	0.98 ± 0.16	0.79 ± 0.13	0.44 ± 0.11
Mean ice melt (km^3 yr^{-1})	330 ± 61.2	389 ± 66.0	214 ± 34.4	203 ± 49.2
Mean ice export (m yr^{-1})	1.55 ± 0.54	0.26 ± 0.38	0.60 ± 0.43	2.34 ± 0.33
Mean ice export (km^3 yr^{-1})	690 ± 243	103 ± 154	163 ± 118	1082 ± 154

TCD
7, 4321–4377, 2013

Table 3. Spatial linear regression of the temporal mean (1985–2011) autumn/winter (April–September) net surface power input to the mixed layer against the temporal mean (1985–2011) autumn/winter: 2 m air temperature, 2 m specific humidity, incoming longwave radiation, incoming shortwave radiation, total precipitation (rain and snow), 10 m zonal (positive eastwards) wind speed, 10 m meridional (positive northwards) wind speed, and summer (January–March) net surface power input, for each of the regions shown in Fig. 9. Each regressed data point corresponds to a specific grid cell and represents the grid point temporal mean value. The coefficient of determination (r^2) is shown in the table, where significant (> 99 %) correlations are highlighted in bold. The sign in the bracket indicates the sign of the respective r value.

P_{net}^{A-S}	Weddell	Bellingshausen	Amundsen	Ross
T_a	**0.24**(–)	**0.27**(–)	**0.14**(–)	**0.54**(–)
Q_a	**0.30**(–)	**0.23**(–)	**0.14**(–)	**0.44**(–)
F_{lw}	0.04 (–)	**0.25**(–)	**0.14**(–)	0.02 (–)
F_{sw}	**0.43**(–)	**0.18**(–)	**0.13**(–)	**0.36**(–)
P	0.00 (+)	0.01 (–)	0.01 (+)	**0.09**(–)
U	**0.18**(–)	**0.21**(–)	**0.09**(–)	**0.08**(–)
V	**0.07**(–)	**0.33**(+)	0.05 (+)	0.00 (–)
P_{net}^{J-M}	**0.55**(+)	0.00 (+)	**0.26**(+)	**0.81**(+)

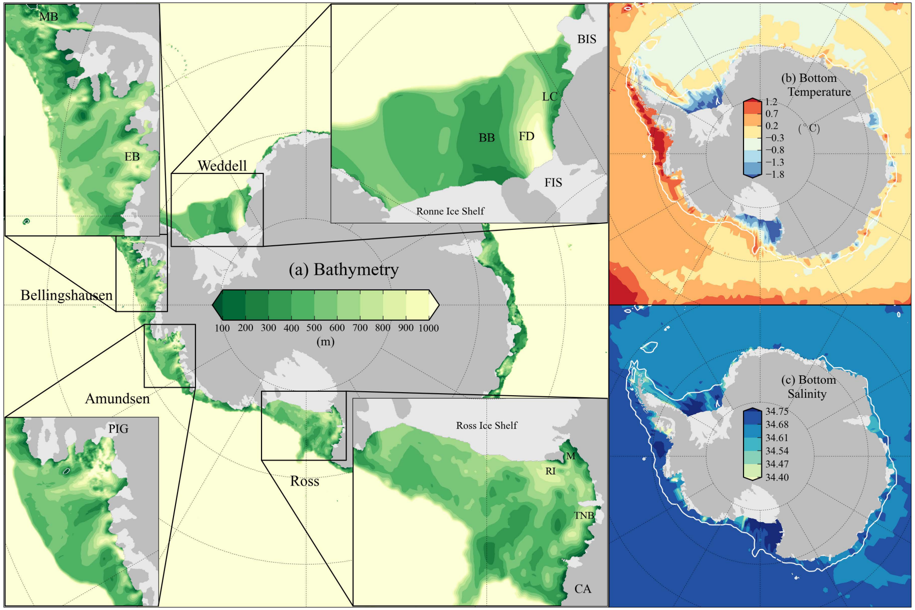

Fig. 1. **(a)** Bathymetry, **(b)** bottom temperature and **(c)** salinity of the Southern Ocean. Bathymetry and landmask are taken from the RTOPO dataset (Timmermann et al., 2010). Ocean data are taken from the World Ocean Atlas (2009) temperature (Antonov et al., 2010) and salinity (Locarnini et al., 2010) datasets. The grey line in **(b)** and **(c)** is the 1000 m isobath contour. BB: Berkner Bank, FD: Filchner Depression, FIS: Filchner Ice Shelf, BIS: Brunt Ice Shelf, LC: Luitpold Coast, MB: Marguerite Bay, EB: Eltanin Bay, PIG: Pine Island Glacier, RI: Ross Island, M: McMurdo Sound, TNB: Terra Nova Bay, CA: Cape Adare.

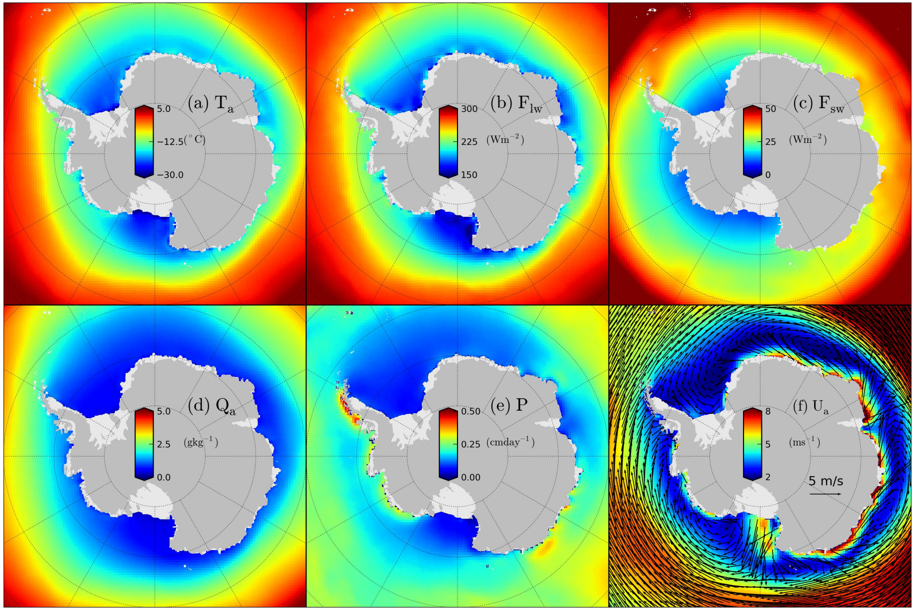

Fig. 2. Mean (1980–2011) ERA-Interim (Dee et al., 2011) winter (JAS) atmospheric forcing. **(a)** 2 m air temperature, **(b)** incoming longwave radiation, **(c)** incoming shortwave radiation, **(d)** 2 m specific humidity, **(e)** total precipitation (snow and rain) and **(f)** 10 m wind speed, overlain with 10 m wind vectors (every third grid point).

TCD
7, 4321–4377, 2013

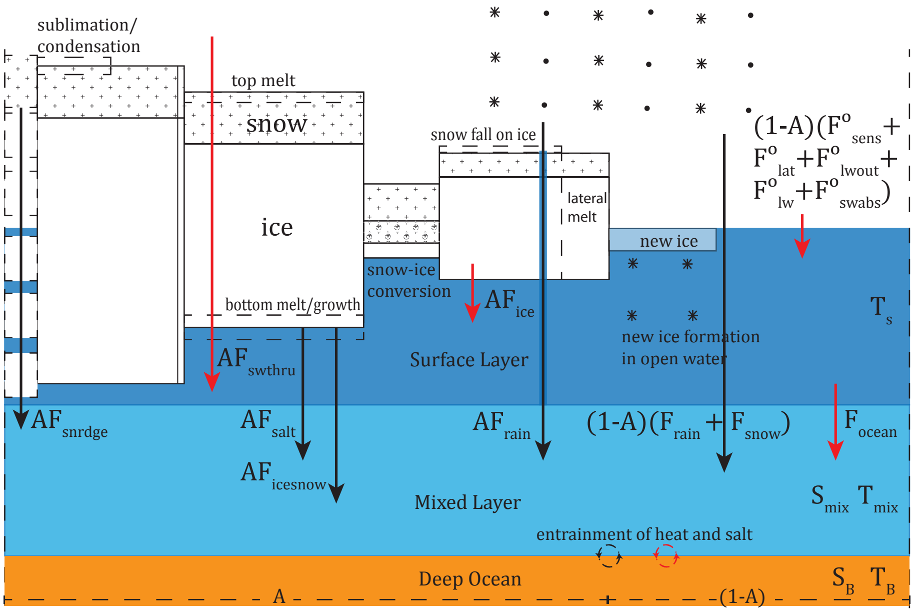

Fig. 3. Schematic of the main thermodynamic processes included in CICE.

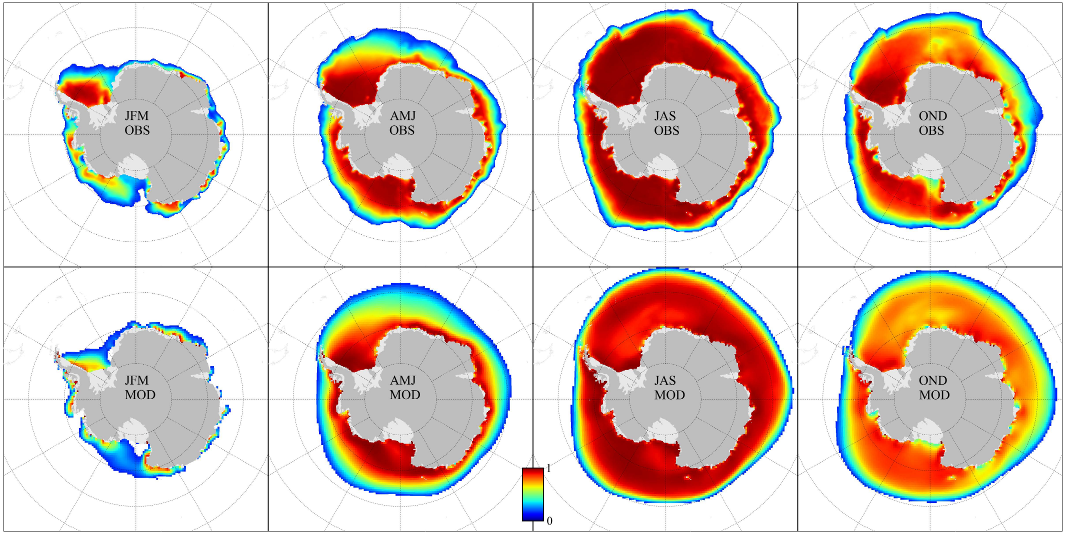

Fig. 4. Mean (1985–2011) seasonal observed (top row) and modelled (bottom row) ice concentration. Ice concentration observations calculated using the Bootstrap algorithm (Comiso, 1999, updated 2012). Ice concentrations less than 0.15 are masked in both datasets.

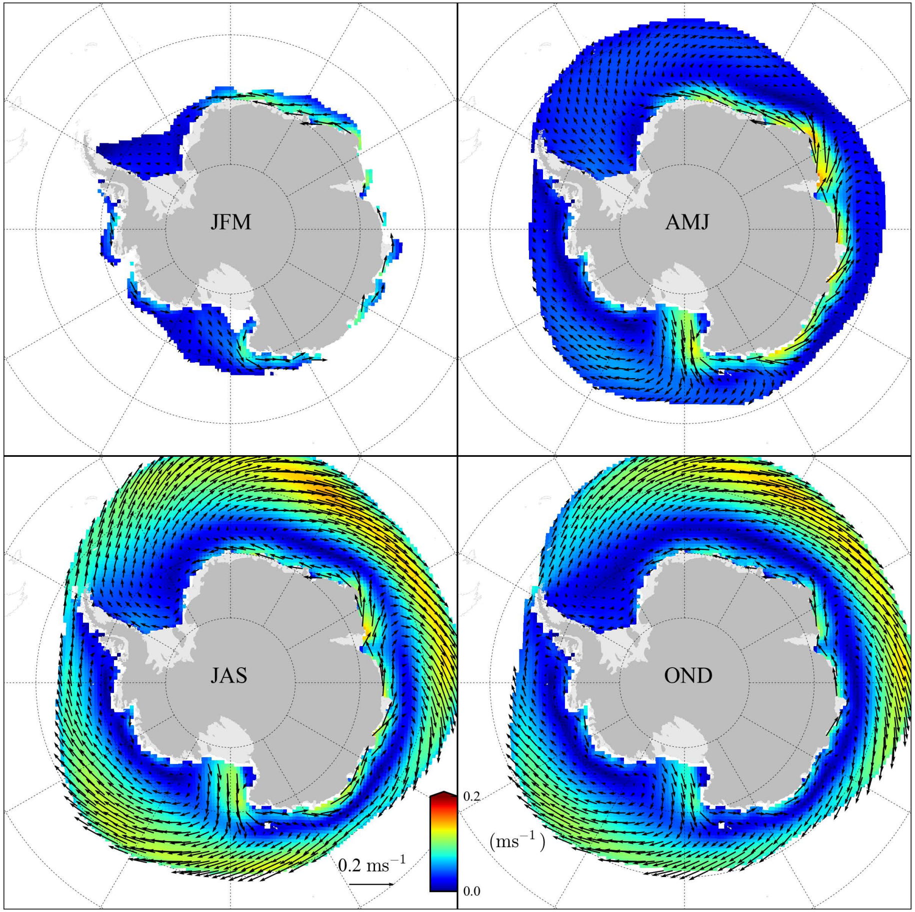

Fig. 5. Mean (1985–2011) seasonal modelled ice motion (ice speed overlain with ice motion vectors). Regions corresponding to a mean ice concentration less than 0.15 are masked in both datasets.

TCD
7, 4321–4377, 2013

Antarctic sea ice and mixed layer

A. A. Petty et al.

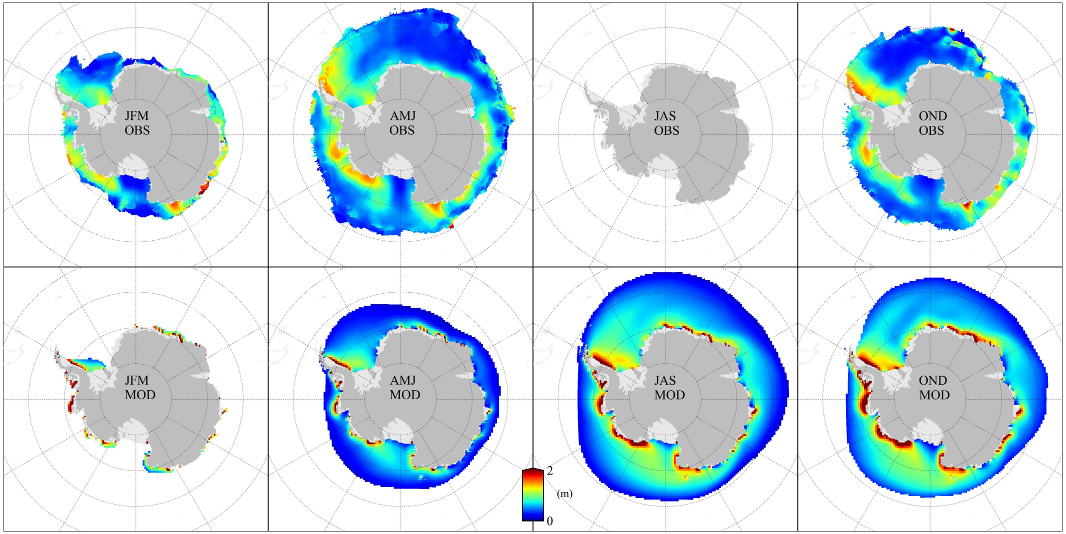

Fig. 6. Mean (1985–2011) seasonal modelled ice thickness (bottom row) compared to mean (2003–2008) seasonal observed ice thickness (top row). Ice thickness observations taken from ICESat measurements (Kurtz and Markus, 2012). Note that no observations were obtained during winter (JAS). Regions with a respective ice concentration less than 0.5 are masked in both datasets.

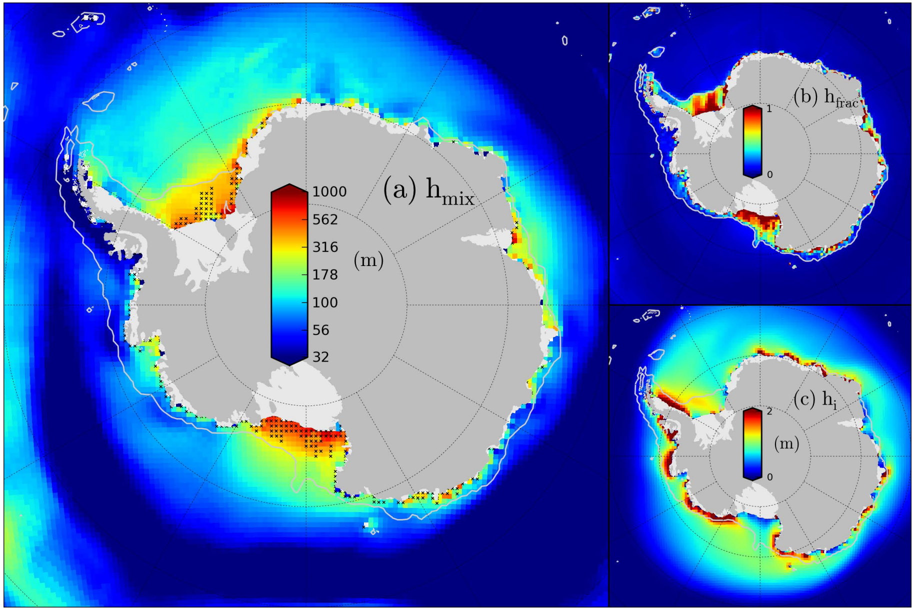

Fig. 7. Mean (1985–2011) **(a)** maximum mixed layer depth, **(b)** fractional depth of **(a)** as a function of the water column depth and **(c)** wintertime (JAS) ice thickness (same as in Fig. 6). Note that the colour scale and colour bar in **(a)** use a logarithmic (base 10) scale.

TCD
7, 4321–4377, 2013

Antarctic sea ice and mixed layer

A. A. Petty et al.

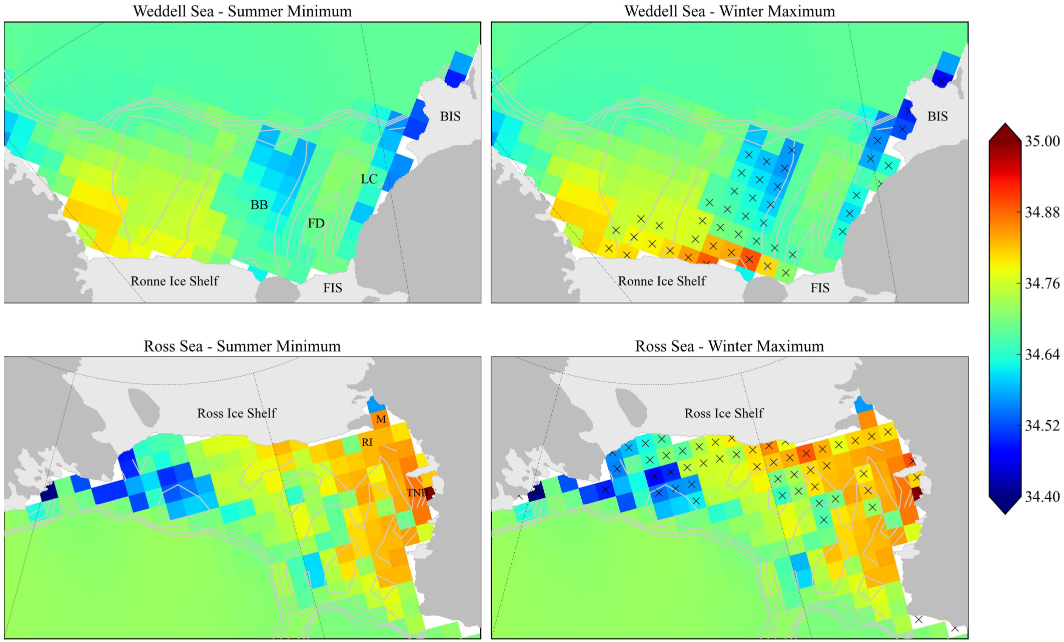

Fig. 8. Mean (1985–2011) modelled summer minimum and winter maximum bottom salinity of the Weddell and Ross shelf seas. The crosses indicate grid cells where the mean maximum mixed layer depth is greater than 90 % of the water column depth.

TCD
7, 4321–4377, 2013

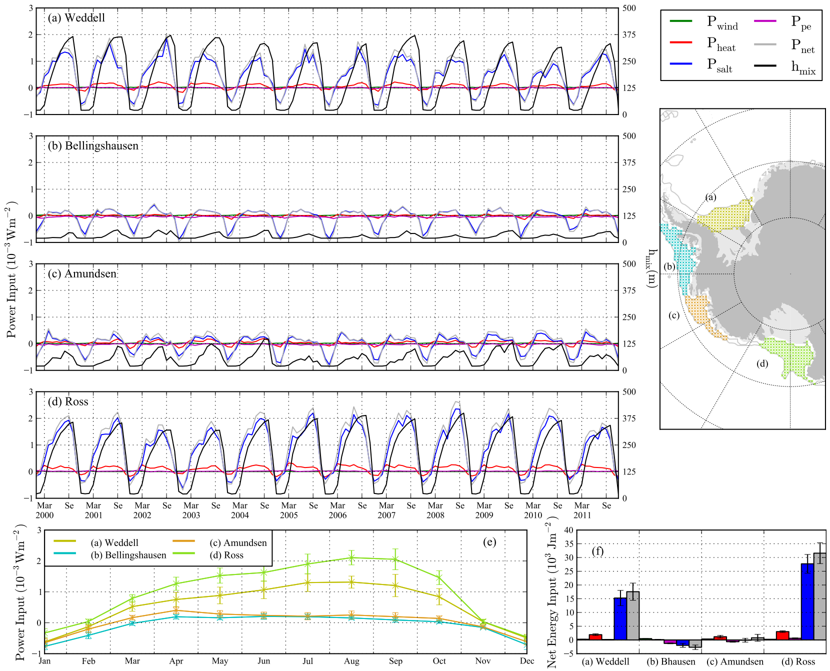

Fig. 9. Mean regional power input to the mixed layer for the years 2000–2011. **(a–d)** power input from wind mixing (green), the ocean-surface layer heat flux (red), the salt flux from sea ice growth/melt (blue), net precipitation minus evaporation (pink), net power input from the addition of all these four terms (grey) and the mixed layer depth (black) averaged spatially over each of the four study regions highlighted in the map shown, **(e)** mean 2000–2011 regional net power input annual cycle, **(f)** mean 2000–2011 regional energy input to the mixed layer from the time integral of each power input term (same colours as **a–d**). The error bars shown in panels **(e)** and **(f)** correspond to one standard deviation form the mean. The surface power inputs are described in Sect.(2.1.2), where we have multiplied by ρ_w to express each term in more suitable units.

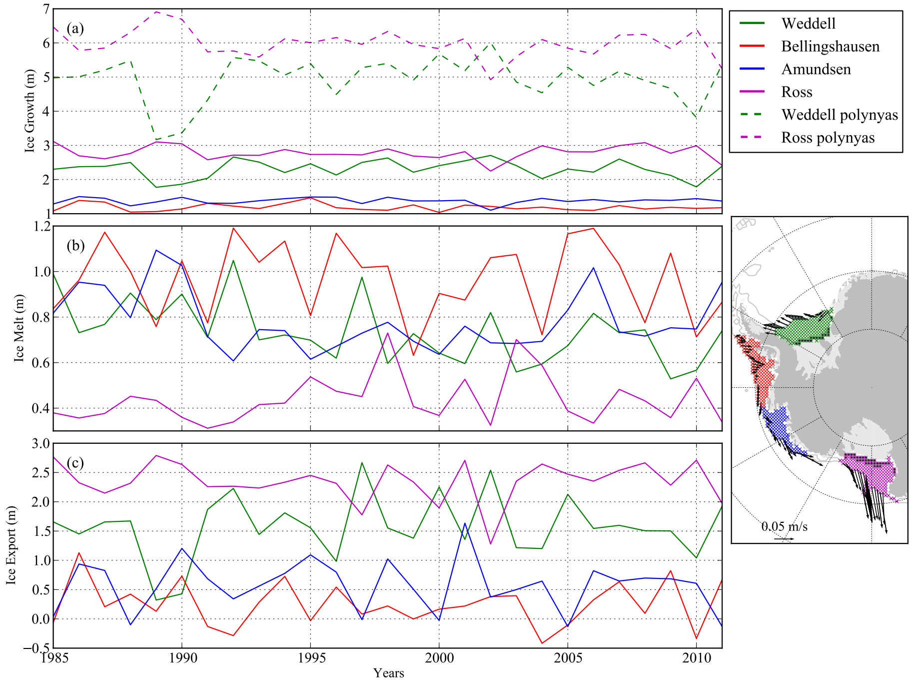

Fig. 10. Annual (1985–2011) regional sea ice mass balance (same regions as Fig. 9). **(a)** Annual regional ice production, including the contribution from rapid sea ice growth "polynya" grid cells (marked by the black crosses), **(b)** annual regional ice melt, **(c)** annual regional net ice export. Mean ice motion vectors for the outer grid cells of each region are shown in the map.

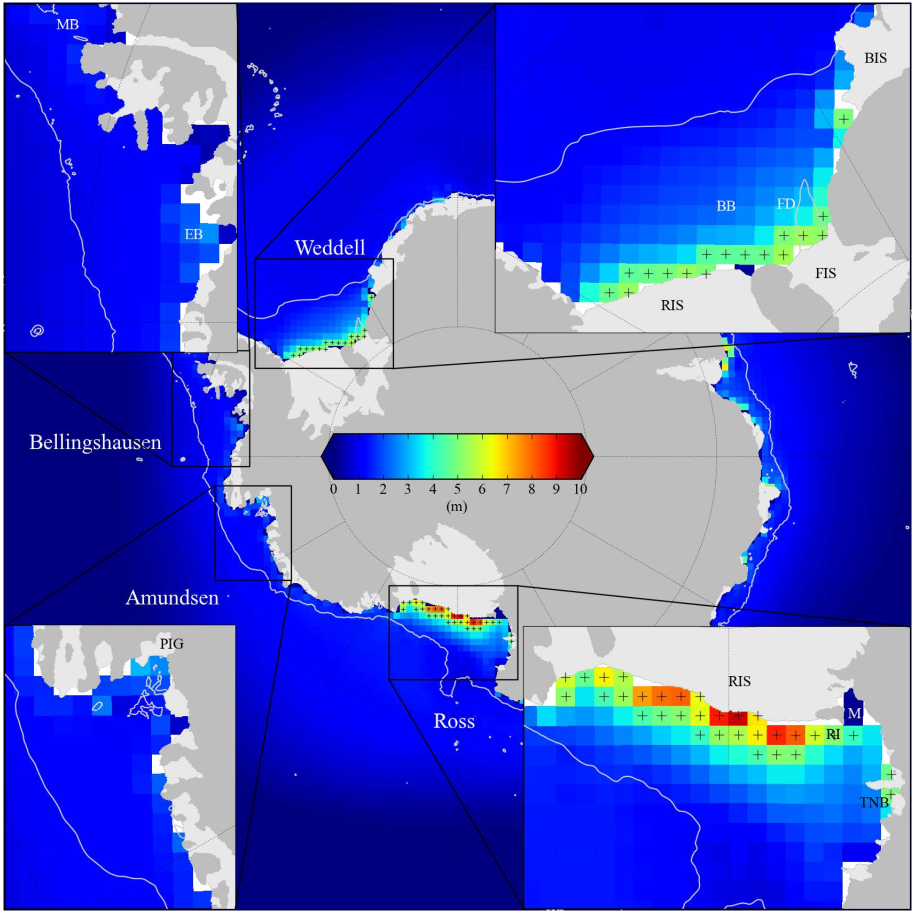

Fig. 11. Mean (1985–2011) annual ice growth. Crosses mark the grid cells where the mean annual ice growth is greater than 4 m.

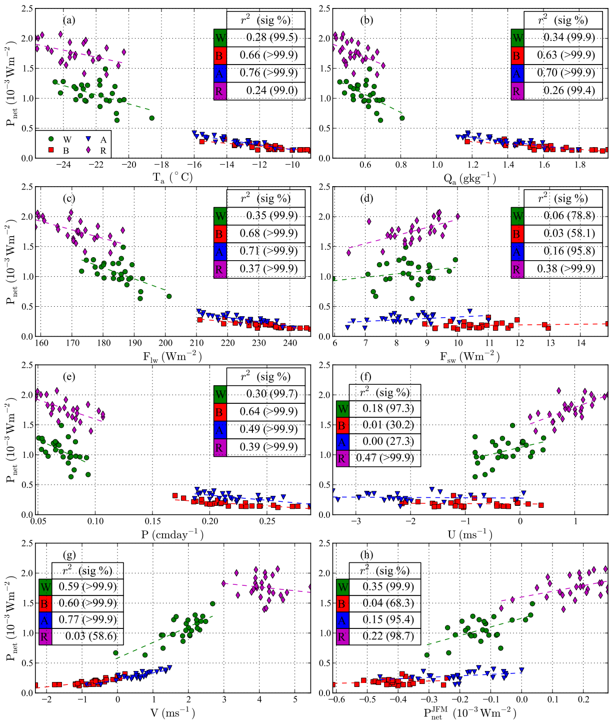

Fig. 12. Linear temporal correlation of the spatial (shelf sea) mean autumn/winter (April–September) net surface power input to the mixed layer against the spatial mean autumn/winter **(a)** 2 m air temperature, **(b)** 2 m specific humidity, **(c)** incoming longwave radiation, **(d)** incoming shortwave radiation, **(e)** total precipitation (rain and snow), **(f)** 10 m zonal wind speed, **(g)** 10 m meridional wind speed and **(h)** summer net surface power input, for the grid points representing each region shown in Fig. 9. Each coloured data point represents a shelf sea and corresponds to the shelf sea annual value. The linear regression lines of each shelf sea dataset are shown by the dashed lines, with the coefficient of determination (r^2) and significance of the correlation shown in the tables within each panel.

TCD
7, 4321–4377, 2013

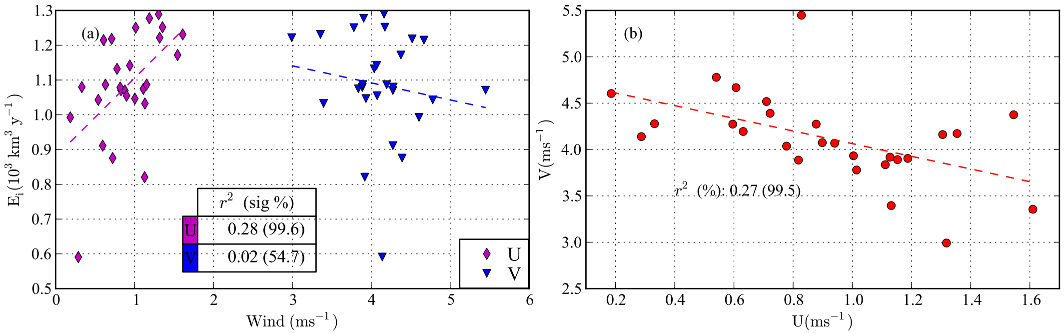

Fig. 13. Linear temporal correlation of the **(a)** annual Ross ice export against the spatial mean autumn/winter 10 m zonal (purple diamonds) and meridional (blue triangles) wind speed, and **(b)** the spatial mean Ross autumn/winter 10 m zonal wind speed against the spatial mean Ross autumn/winter 10 m meridional wind speed. Each data point corresponds to the Ross shelf annual value.

TCD
7, 4321–4377, 2013

Antarctic sea ice and mixed layer

A. A. Petty et al.